Leakage Flux Modeling of Medium-Voltage Phase-Shift Transformers for System-Level Simulations

M. Luo, D. Dujic, and J. Allmeling

Leakage Flux Modeling of Medium-Voltage Phase-Shift Transformers for System-Level Simulations

Min Luo, *Member, IEEE,* Drazen Dujic, *Senior Member, IEEE,* and Jost Allmeling, *Member, IEEE*

Abstract—Cascaded H-Bridge converters in medium voltage applications have all the DC link capacitors supplied from external source through a multi-winding phase-shift transformer. This type of transformers has a complex winding geometry, which leads to unbalanced leakage flux paths. The unbalance affects the dynamic behaviour of the converters. This work proposes a modeling approach which realistically captures the unbalance in the leakage flux path of phase-shift transformers, using permeance magnetic circuit. The model can be seamlessly integrated into system-level simulation of power electronic circuits. Taking advantage of the repetitive structure of the windings, the model requires very limited number of parameters, which can be easily obtained from the geometry data together with only a few experimental tests. The fidelity of the model is experimentally confirmed on a phase-shift transformer from a commercial medium-voltage drive system.

Index Terms—leakage flux modeling, phase-shift, dynamic, system-level simulation, magnetic circuit, permeance-capacitance

NOMENCLATURE

W_p	Primary winding.
N_p	Primary winding number of turns.
V_p	Primary winding voltage.
I_p	Primary winding current.
W_s	Secondary windings.
N_s	Secondary winding number of turns.
V_s	Secondary winding voltage.
I_s	Secondary winding current.
$\mathscr{P}$	Magnetic permeance.
μ	Magnetic permeability.

I. INTRODUCTION

Phase-shift transformers are widely used in medium voltage AC to AC converter systems to interface the power grid. These types of transformers usually have multiple secondary winding groups supplying line-commutated rectifiers. They are configured to be star-, delta-, or mixed connections which generate different phase-shift angles. In order to achieve optimal harmonic cancellation of the grid current on the primary winding side, the phase-shift angles referenced to the primary phase voltage are usually chosen as [1]

M. Luo and D. Dujic are with the Power Electronics Laboratory, École Polytechnique Fédérale de Lausanne (EPFL), Lausanne, CH-1015 Switzerland (e-mail: min.luo@epfl.ch, drazen.dujic@epfl.ch).
J. Allmeling is with Plexim GmbH, Zürich, CH-8005 Switzerland (e-mail: allmeling@plexim.com).
Manuscript received July 16, 2017; accepted May 8, 2018.

$$\theta = 60° \cdot (K - 1)/N - 30° \qquad (1)$$

where N is the total number of secondary winding groups, and $K = 1...N$ the index of the secondary winding groups. Among the MV converter systems using phase-shift transformers, one typical topology, the cascaded H-bridge (CHB) converter, patented by Robicon Corporation [2] has become popular in medium voltage (MV) drive applications. CHB converter has the advantages such as good fault-tolerance ability [3], and in particular, simplicity as well as rather low cost due to the ability to realise medium voltage drive using low voltage semiconductors. This type of converter is composed of multiple power cells as depicted in Fig. 1. Each power cell consists of a three-phase diode rectifier and a single-phase H-bridge inverter. The phase-shift transformer is used to provide isolated AC voltage sources for each of the rectifiers. In order to improve the harmonic content of the voltage and reduce the switching frequency on the inverter output, high number of power cells are desired so that the phase-shift transformer usually has a large number of secondary windings. In such a kind of transformer, non-identical position of the individual windings may lead to different leakage flux coupling, which gives rise to unbalanced short-circuit impedances [4]. This unbalance is directly reflected in the dynamic behaviour of the converter system, especially the current flowing out of the secondary winding groups, which directly determines the winding loss as well as the selection of the rectifier diodes including their cooling design. Moreover, the ripple current of the DC-link capacitors is also influenced. The analysis made in [5] demonstrated that the leakage inductance of the phase-shift transformer has direct contribution to the ripple current of the DC-link capacitors in CHB converters, which highly affects the capacitors' lifetime [6].

Using accurate transformer models which can be combined with power electronic circuit for system-level dynamic simulation, the potentially negative effect of the unbalance can be evaluated conveniently. From the simulation results, the appropriate components can be selected for the converter system, and the control algorithm as well as protection method can be optimized.

The leakage flux distribution of the individual windings can be accurately captured by finite element method (FEM). However FEM is not optimal for dynamic simulation combined with complex power electronic circuits, due to its high computational effort and poor convergence in these circumstances.
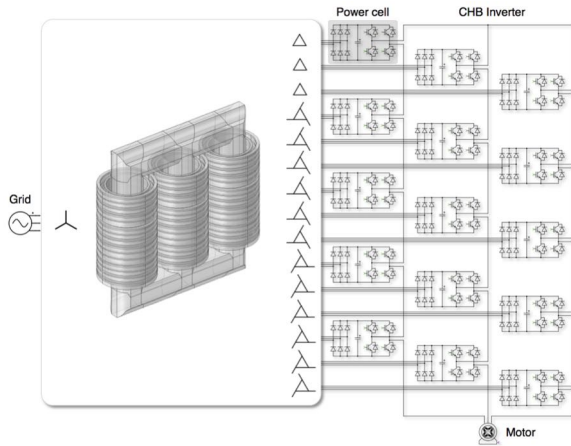
Fig. 1: Typical topology of cascaded H-bridge converters in MV drive application.
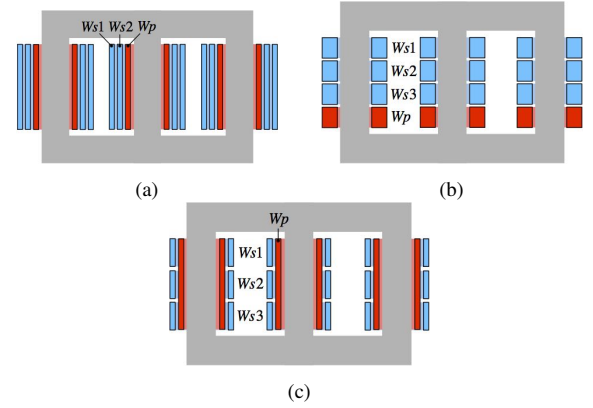

Fig. 2: Winding arrangements considered in the existing publications (a) Multilayer; (b) Multidisk; And the special arrangement in the transformer of CHB converters; (c) Mixed.

Instead, transformers are commonly represented by electrical equivalent circuit using coupled inductors in system-level simulation. In order to identify all the self- and mutual inductance values including the main flux- and leakage flux path, electric test is required to be enumerated among different short-and open circuit combinations, which can be time consuming and in some cases impractical. It is especially the case if more than two windings are present, like the phase-shift transformer in CHB converters.

Magnetic circuit representation using permeance or reluctance has become popular nowadays as alternative to FEM and coupled-inductor model, regarding the following advantages

- The complexity is much lower than FEM thanks to the lumped representation
- Magnetic circuit has closer relation to the geometry than coupled-inductor
- The integration to electrical circuit is nearly seamless

In combination with the material characteristic, this methodology has been successfully applied to model the main flux path [7]–[11]. However, the leakage flux path was not analyzed in these studies.

Due to the difficulty in parametrisation, only a few publications have considered the leakage flux path in the magnetic circuit. In a magnetic circuit approach it is assumed that the fluxes are confined in virtual tubes. The tube can be separated into sections, and each of them is characterised by the geometry together with the material's permeability μ as a lumped reluctance or permeance. Since the geometry of the main flux path through the iron core is determined and directly visible, the parametrising is straightforward. In comparison however, the geometry of the leakage flux path through the air is usually not intuitively shaped.

Some of the publications have parametrised the leakage flux path directly using geometrical information. In the work of [12] and [13], the authors managed to parametrise the leakage flux path in similar manner as the main flux path, thanks to the special core-structure of the magnetic components taken for study. In this case, the geometry of the leakage flux path was well determined, which however, can hardly be generalised.

For transformers with typical core structures, the authors of [14] have presented a generalised reluctance magnetic circuit including the leakage flux path between the windings for complex multi-winding structures, which was further adopted by the work in [15] and [16] for dynamic simulation. In that work, the magnetic circuit served as a intermediate step to derive the terminal-duality model (TDM) introduced by [17], which was essentially electrical equivalent circuit with coupled inductances including the leakage flux path. For parametrisation however, large number of electric tests can not be avoided, since the elements of the leakage inductance matrix are linear summation of the short-circuit impedances between certain winding pairs. In order to get rid of the electric tests, authors of [18] calculated the short-circuit impedances between winding pairs directly from geometrical data using the method introduced in [19]. The simulated short-circuit impedance matched well to the experimental measurements from single- and three phase transformers. However the increased error in the three-phase case indicates that the 2D formulation of the method from [19] may run into issues, if the part of windings outside the core window area (not between the core limbs) dominates, as is the case in the phase-shift transformer of CHB converters. Moreover, among the three-phase transformers modelled by the existing publications, only the multilayer- (Fig. 2a) and multidisk- (Fig. 2b) winding arrangements have been covered, while the mixed one (Fig. 2c) present in the transformers in CHB converters is not discussed.

The leakage flux models with direct parametrization from geometry are difficult to generalize accurately, while the ones parametrised from electric test do not include the geometrical information contained in the magnetic circuit, so that a large measurement effort is needed. In our previous work in [20], we have proposed a magnetic circuit based on a permeance-capacitor analogy [21], which combines the intuitive geometric information and experimental results from only a few electric tests together. The accuracy of the magnetic circuit has been verified on a single-phase multi-winding transformer prototype under short-circuit test and operation with single-phase rectifier connections.

In comparison to [20], this work has been significantly extended in the following aspects:

- The methodology of modelling the leakage magnetic flux path is extended to three-phase case of the phase-shift transformers in CHB converters, the fidelity of which is verified on a real transformer from a commercial product.
- In the magnetic structure discussed [20], the secondary windings were placed with the same interval in between and the primary winding was aligned with them vertically. In this work, the non-idealities of extra gap between some of the secondary windings and unaligned primary winding position are also covered, which exist in the reality due to design insulation coordination.
- The intuitive representation of complex phase-shift winding configuration using gyrator structure in permeance-based magnetic circuit is demonstrated, which was not covered by the single-phase case.
- An analytical explanation is provided for the physical origins of the unbalanced leakage flux coupling versus the position of the windings.

In section II, model with ideally balanced leakage flux path is established including the representation of complex winding configuration. Then in section III, the physical origins of the unbalanced leakage flux coupling in reality is analysed using a simple multi-winding magnetic structure. Afterwards in section IV, the improved model with unbalanced coupling is described, followed by the experimental verification via short-circuit tests in section V and connection to diode rectifiers in VI. Finally in section VII the application of the proposed model in system-level simulation of the whole power converter system is demonstrated, and the result is compared to that from the model with ideally balanced leakage flux coupling.

II. MODEL WITH IDEALLY BALANCED LEAKAGE FLUX

An available phase-shift transformer from a commercial MV drive system supplying a CHB inverter is taken as a study case. The modeling is carried out only based on the nameplate data as well as the measurable geometrical- and electrical characteristics, since the detailed internal design specification of this transformer is not provided by the manufacturer. The rated parameters from the nameplate are listed in TABLE I.

TABLE I: Rated parameters of the MV phase-shift transformer

Parameter	Value	Parameter	Value
Apparent power	1MVA	Primary current	96.2A
Frequency	50Hz	Secondary voltage	710V
Primary voltage	6.3kV	Secondary current	54.2A

The geometrical structure of the transformer has been depicted in Fig. 3a, which is composed of a three-limb laminated core, one primary winding and 15 secondary windings. The secondary windings are stacked vertically in succession and wound concentrically around the long primary winding on each of the three legs, they are divided into three groups denoted by A, B and C. Within each of the three groups, the secondary windings numbered with 1~5 are made up of multiple electrically isolated sub-windings that are connected
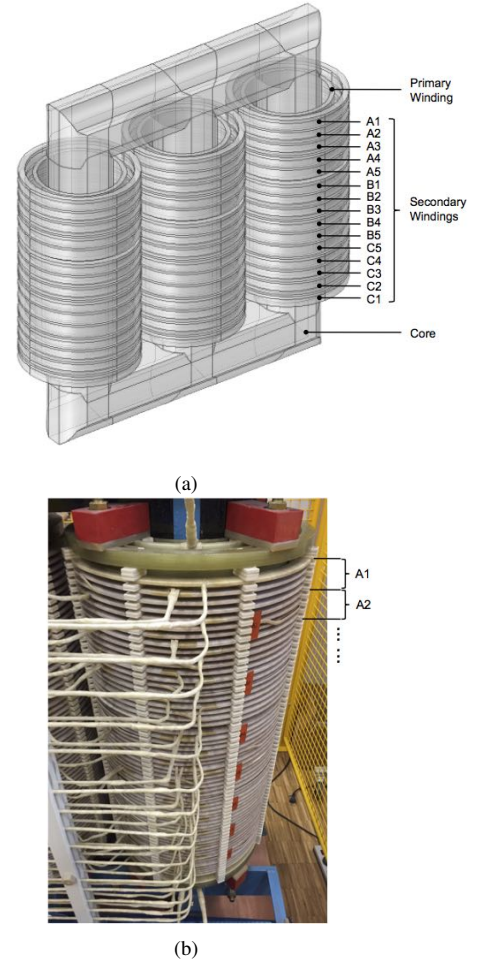

(a)

(b)

Fig. 3: Structure of the phase-shift transformer with one primary- (W_p) and 15 secondary windings ($W_{s,A1}...W_{s,A5}$, $W_{s,B1}...W_{s,B5}$, $W_{s,C5}...W_{s,C1}$): (a) 3-D draft; (b) Photo of the secondary windings of input phase "w".

in different configurations to get the desired phase shifts. The basic model can be established as shown in Fig. 4b. The three-leg iron core is modelled as magnetic circuit in an intuitive way, the permeance blocks $P_{C,limb}$ represent the three limbs, while $P_{C,yoke}$ represent the yokes together with the corners. The permeance values can be calculated using the formula introduced by [22] with the geometrical parameters of the transformer core (marked in Fig. 4a).

$$P_{C,limb} = \mu_C \cdot \frac{A_C}{h_{limb}} \quad (2)$$

$$P_{C,yoke} = \mu_C \cdot \frac{A_C}{h_{yoke} + (h_x + dx) \cdot \pi/4} \quad (3)$$

where μ_c is the permeability of the core material and A_c the cross-section area of the core limb and yoke. These informations are usually directly available, either from the datasheet of the manufacturer or via measurement of geometry.

The gyrator structure demonstrated in Fig. 5 is adopted to represent the windings of the transformer, which serves as
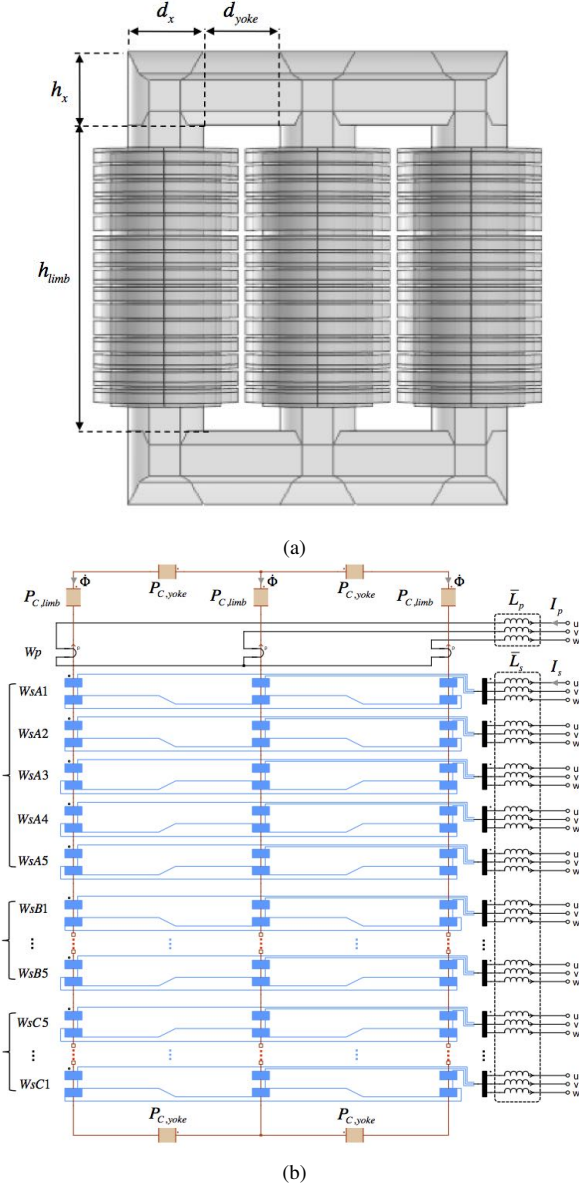
(a)

(b)

Fig. 4: (a) Core geometry of the transformer; (b) Model of the transformer including magnetic- and electrical circuit with ideally balanced leakage inductances.

interface between the magnetic- and electrical circuit. The primary winding W_p is modelled as three simple gyrator blocks, which are star-connected in the electrical circuit. Each secondary winding is composed of six gyrator blocks with interconnection in the electrical circuit, as depicted in Fig. 6, which represent the star- (turns number $N_{s,Y}$) and delta part (turns number $N_{s,\Delta}$) of the mixed connection, respectively.
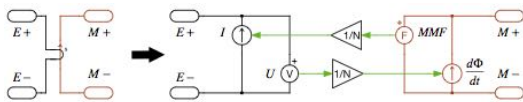

Fig. 5: Gyrator structure of the winding component

The gyrator representation significantly facilitates the modeling thanks to the intuitive geometrical relation to the real transformer, without the need of deriving a complex electrical equivalent. $N_{s,Y}$ and $N_{s,\Delta}$ of all the secondary windings can be counted from the real transformer directly, which account for different phase-shift angles referring to the primary side, as has been listed in TABLE II.

Please note that the winding resistance is series connected in the electrical part of the circuit, for star- and delta part of the winding, respectively. The resistance value R_w can be approximated as

$$R_w = \rho_{cu} \cdot l_w / A_w \qquad (4)$$

where ρ_{cu} is the resistivity of copper, l_w is the conductor length of the star- or delta part of the winding, and A_w is the conductor cross-section area. l_w and A_w can be directly obtained from the real transformer.

The magnetic circuit together with the winding components have covered the main magnetic flux path which is constrained inside the iron core. The interface behavior on the winding terminals is equivalent to the conventional electrical circuit model using coupled inductors. The leakage flux path however, is still missing. In order to introduce the leakage flux path into the circuit, one conventional way is to connect electrical inductors $\overline{L}_p$ and $\overline{L}_s$ in series with the winding terminals, which represent the leakage inductance of the primary- and secondary windings, respectively, as shown in Fig. 4b. For simplification, the same inductance value $\overline{L}_s$ can be assigned to the inductors connected to the secondary windings. $\overline{L}_p$ and $\overline{L}_s$ are given using the equations below, as an approximation.

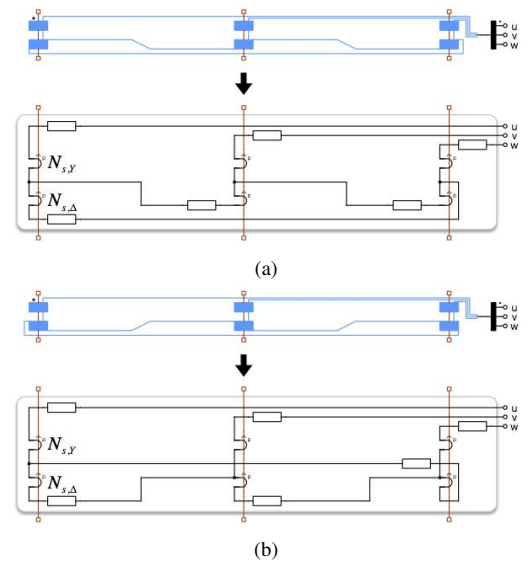$$\overline{L}_p = L_{k,Test}/2 \qquad (5)$$

(a)

(b)

Fig. 6: Magnetic- and electrical circuit model of the secondary winding (a) with positive phase shift; (b) with negative phase shift.

TABLE II: Phase-shift and turns number of the secondary windings

	$W_{s,A1(B1,C1)}$	$W_{s,A2(B2,C2)}$	$W_{s,A3(B3,C3)}$	$W_{s,A4(B4,C4)}$	$W_{s,A5(B5,C5)}$
Angle	$+18°$	$+6°$	$-6°$	$-18°$	$-30°$
$N_{s,Y}$	15	30	30	15	0
$N_{s,\Delta}$	40	13	13	40	64

$$\overline{L}_s = (L_{k,Test}/2) \cdot 15 \cdot (710/6300)^2 \qquad (6)$$

L_k is the equivalent inductance looking into the primary winding, which is measured from the test scheme with the primary winding supplied and all the secondary windings short-circuit at the same time. $6300V$ and $710V$ are the nominal voltage (TABLE I) of the transformer's primary and secondary side, respectively. Here it is assumed that the leakage flux path of the individual windings are identical and totally decoupled from each other. This assumption, which is usually made in practice and make the ideal model rather simple, is however not representative enough of the real transformer. In reality, the windings are not only linked via the flux path inside the iron core, but also via the leakage flux path through the air. The strength of the air-path linkage between the windings is strongly influenced by the relative positioning, this will result in unbalanced leakage inductance looking into the individual windings. In the following sections of the work, this unbalance is demonstrated in experimental test, and the modeling's approach covering the unbalance in leakage flux path is introduced.

III. ORIGINS OF UNBALANCED LEAKAGE FLUX

Prior to further introducing the improved model of the phase-shift transformer, the physical background of the unbalance in magnetic flux coupling is analysed using a simplified single-phase transformer. As depicted in Fig. 7a, the single phase transformer is composed of one primary winding W_p which spreads out the middle limb of the iron core, as well as M identical secondary windings W_{s1} ~W_{sM} stacking over each other. The magnetic circuit topology proposed by [20] defines a virtual tunnel network for the magnetic flux according to the real geometry, which is adopted for the analysis as demonstrated in Fig. 7b. Considering the axis-symmetry of the geometry, the left- and right halves of the original magnetic circuit can be merged together. Following the formulation of [20], all divisions of the leakage flux path share the same three permeance values P_s, P_{long} and P_{shunt}. The vertical leakage permeances (P_s, P_{long}) surrounding the primary- and secondary windings stand for the leakage paths looping back to the corresponded limb, the flux flowing through P_s only links with the primary winding section, while that through P_{long} links the primary- and secondary windings together. The horizontal ones (P_{shunt}) stand for the leakage paths between different limbs. If the permeance representing the core limbs (P_{mid} and P_{side} in Fig. 7b) are significantly larger than that of the leakage ones, they can be replaced by short-circuit lines, as shown in Fig. 7c. The permeance representing the core yokes (P_{yoke}) in Fig. 7c can be merged with the horizontal permeances P_{shunt} at the top and bottom

of the magnetic circuit, yields the the equivalent permeance $P'_{shunt} = P_{shunt} + P_{yoke}$ in Fig. 7c. The primary winding has been equally divided into M sections, the effect of an AC current I_p flowing on the primary winding can be represented by M identical MMF sources connected in each division, whose value is given by

$$F'_p = I_p \cdot N_p/M \qquad (7)$$

where N_p is the turns number of the primary winding. If the secondary winding are kept open, the induced magnetic flux rate $\dot{\Phi}_{s1}$~$\dot{\Phi}_{sM}$ ($d\Phi/dt$) are essentially the "magnetic" current flow on the corresponding branches, as has been highlighted in Fig. 7c. In order to derive $\dot{\Phi}_{s1}$~$\dot{\Phi}_{sM}$, the circulating flux rate $\dot{\Phi}_1$~$\dot{\Phi}_M$ in each division are firstly calculated. Following the second Kirchhoff's law applied to magnetic circuit, the flux rates in the very top- and very bottom division are given by

$$F'_p = (X'_{shunt} + X_{shunt}) \cdot \dot{\Phi}_1 - X_{shunt} \cdot \dot{\Phi}_2 \qquad (8)$$

$$F'_p = (X'_{shunt} + X_{shunt}) \cdot \dot{\Phi}_M - X_{shunt} \cdot \dot{\Phi}_{M-1} \qquad (9)$$

where X is the "magnetic" reactance equal to $1/(\omega \cdot P)$ with ω standing for the angular frequency of the primary current I_p. For the divisions in between with the index $1 < m < M$, the relations comply to

$$F'_p = 2 \cdot X_{shunt} \cdot \dot{\Phi}_m - X_{shunt} \cdot \dot{\Phi}_{m-1} - X_{shunt} \cdot \dot{\Phi}_{m+1} \quad (10)$$

equation (8) and (9) can be reorganised as

$$\dot{\Phi}_2 - \dot{\Phi}_1 = \frac{-F'_p + X'_{shunt} \cdot \dot{\Phi}_1}{X_{shunt}} \qquad (11)$$

$$\dot{\Phi}_M - \dot{\Phi}_{M-1} = \frac{F'_p - X'_{shunt} \cdot \dot{\Phi}_M}{X_{shunt}} \qquad (12)$$

On one hand, the vertical symmetry of the magnetic structure leads to the fact that $\dot{\Phi}_1 = \dot{\Phi}_M$, which can be substituted into (11) and (12), thus one can easily find out

$$\dot{\Phi}_2 - \dot{\Phi}_1 = -(\dot{\Phi}_M - \dot{\Phi}_{M-1}) = \Delta\dot{\Phi}_1 \qquad (13)$$

On the other hand, reformatting equation (10) yields the recursive expression

$$\Delta\dot{\Phi}_m - \Delta\dot{\Phi}_{m-1} = (\dot{\Phi}_{m+1} - \dot{\Phi}_m) - (\dot{\Phi}_m - \dot{\Phi}_{m-1}) = -\frac{F'_p}{2 \cdot X_{shunt}} < 0 \qquad (14)$$

Combining the equations (13) and (14) together, the difference between the circulating flux rate of adjacent divisions
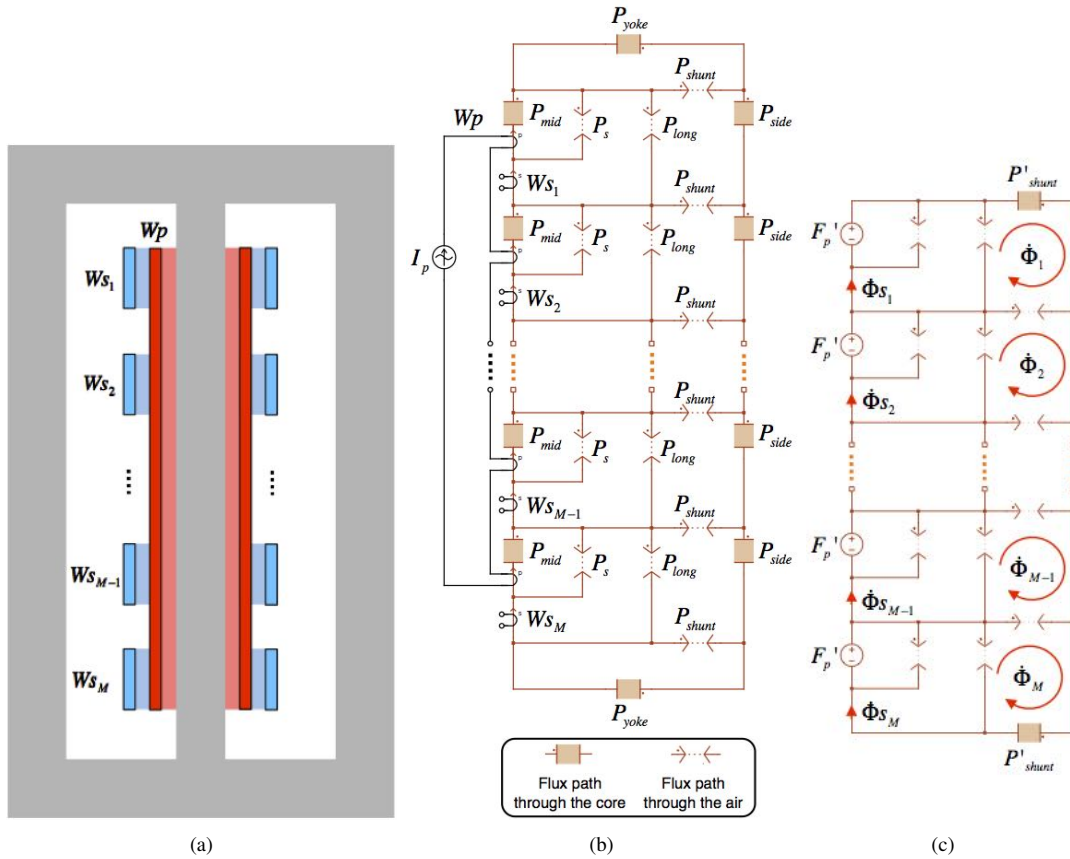
Fig. 7: Demonstration of the unbalanced coupling I (a) Single phase transformer with M secondary windings; (b) Magnetic circuit of the transformer with current I_p flowing on the primary winding and all secondary windings are left open; (c) Simplified magnetic circuit where the core limb permeances are neglected and the two yoke permeances are merged into P_{shunt} as P'_{shunt}.
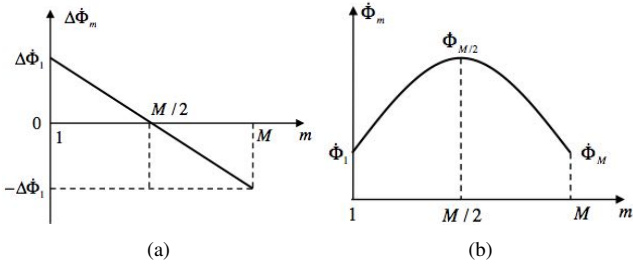

Fig. 8: (a) Difference between the circulating flux rate of adjacent divisions against the division index; (b) Circulating flux rate of adjacent divisions against the division index.

turns out to be a linear function of the division index which crosses zero at $m = M/2$, as demonstrated in Fig. 8a. Despite the discrete form, this linear function can be considered as *derivative* of the circulating flux rate $\dot{\Phi}_m$ itself against index m, thus $\dot{\Phi}_m$ turns out to be a second-order polynomial having the maximum at $m = M/2$, as demonstrated in Fig. 8b. The flux rate $\dot{\Phi}_{s(m)}$ of the individual secondary windings is constantly biased from the corresponding circulating flux rate $\dot{\Phi}_m$, given as

$$\dot{\Phi}_{s(m)} = \dot{\Phi}_m + \frac{F'_p}{X_{long}} \qquad (15)$$

Therefore $\dot{\Phi}_{s(m)}$ is also a second-order polynomial and the maximum of which also take place at the secondary winding with index $M/2$, that is at the middle of the primary winding. This reveals the fact that the closer the secondary winding is placed to the centre of the primary winding, the better the flux coupling can be obtained.

After the analysis of the coupling between primary- and secondary windings, the coupling on the secondary side can be demonstrated under the assumption that an AC current I_s is flowing on the secondary winding W_{s1}, while all the other secondary windings $W_{s2} \sim W_{sM}$ as well as the primary winding are left open, as illustrated in Fig. 9a. After the same simplification made in the previous analysis case as well as replacing the open windings with short circuit lines, the magnetic circuit becomes the structure shown in Fig. 9b. The induced flux rates on the secondary windings $\dot{\Phi}_{s1} \sim \dot{\Phi}_{sM}$ as well as that flowing on the horizontal permeances $\dot{\Phi}_{h1} \sim \dot{\Phi}_{h(M-1)}$ have been denoted in Fig. 9b, following the first Kirchhoff's law yields
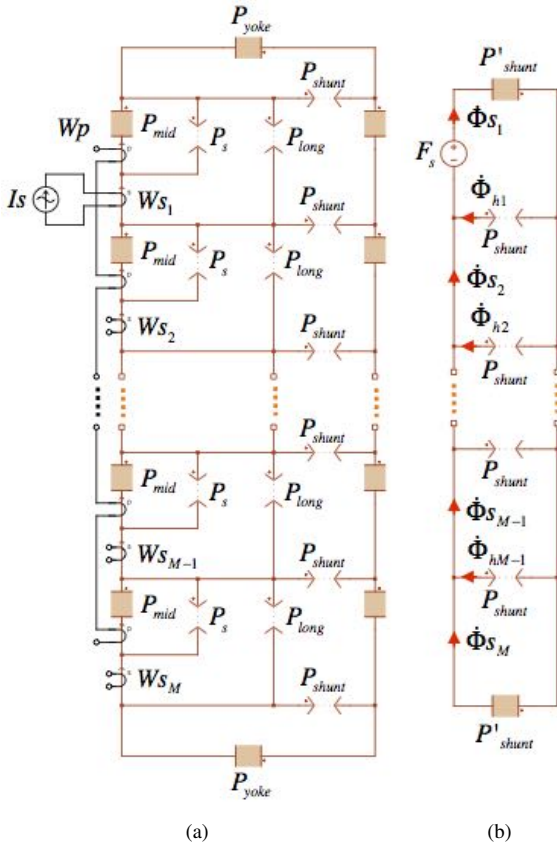
(a) (b)

Fig. 9: Demonstration of the unbalanced coupling II (a) Magnetic circuit of the transformer with current I_s flowing on the secondary winding W_{s1} and other secondary windings as well as the primary winding are left open; (b) Simplified magnetic circuit where the core limb permeances are neglected and the two permeances P_{yoke} representing the core yoke are merged into P_{shunt} (P'_{shunt}).
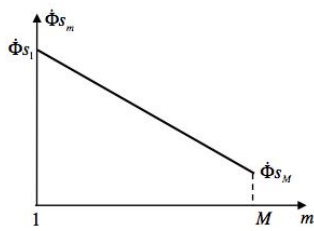

Fig. 10: Flux rate of secondary windings against the division index.

$$\dot{\Phi}_{s(m+1)} = \dot{\Phi}_{s(m)} - \dot{\Phi}_{h(m)} \qquad (16)$$

Since the horizontal flux rates $\dot{\Phi}_{hm}$ are greater than zero and they have the same value in all the divisions (due to the same horizontal permeance value P_{shunt}), a linear function can be used to describe the distribution of the secondary winding flux rates $\dot{\Phi}_{h(m)}$ with respect to the winding index, as demonstrated in Fig. 10. The relation $\dot{\Phi}_{s(m+1)} < \dot{\Phi}_{s(m)}$ indicates the fact that the closer the secondary winding is located to W_{s1}, the

better flux coupling is present. All the phenomenon from the analysis above has been observed from the experimentally measured short-circuit impedance of a single-phase prototype transformer in [20] and is further proved by this work on a three-phase transformer in a later section as well.

IV. MODEL WITH UNBALANCED LEAKAGE FLUX

In the case of phase shift transformer, the model of unbalanced leakage flux path is established by extending the magnetic circuit of the ideal model with leakage permeances, instead of connecting identical inductors in the electrical circuit. Similar to the single-phase prototype transformer which was discussed in the work of [20], here the primary winding is also distributed over the length of the core limbs, while the secondary windings are stacked vertically in succession. Recall that the modeling's approach proposed by [20] requires that the secondary windings have repetitive structure, so that only a few number of permeance values are required to parametrise the leakage flux path. This requirement is fullfilled in the phase-shift transformer as well. As marked in Fig. 3b,
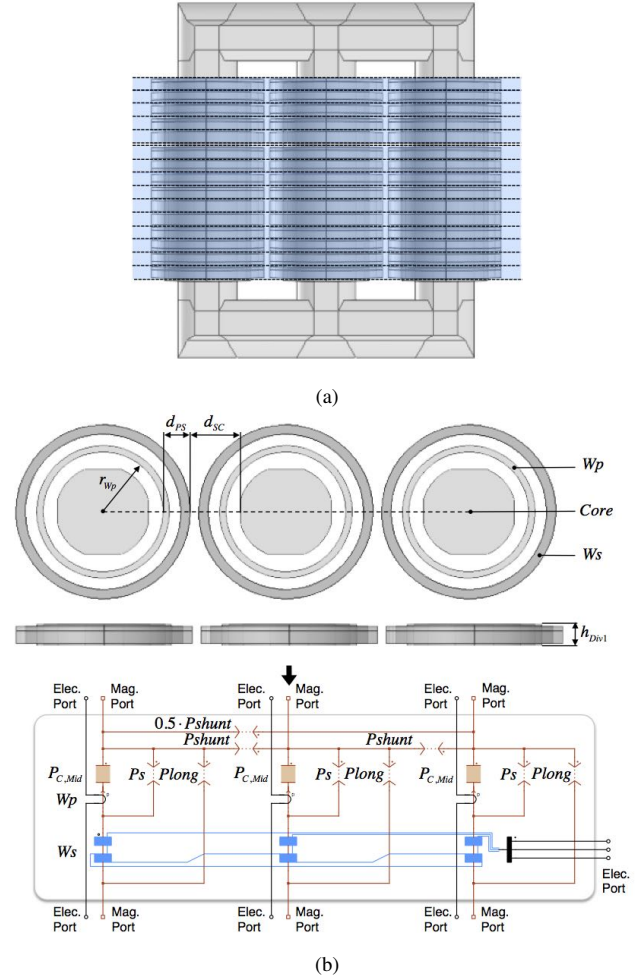

(a)

(b)

Fig. 11: Divisions of type 1 (a) Position in the transformer; (b) Cross section and permeance magnetic circuit with the flux path of the core and air.

Fig. 12: Type 1 division including secondary winding W_{sA1} with shorter primary winding section.

one single phase of each secondary windings is composed of four conductor bundles (in Fig. 3a they are displayed as one solid block), the overall height and radius of the four bundles together are approximately identical between different secondary windings. In this sense, the modeling of the phase-shift transformer using permeance-capacitor based magnetic circuit can be carried out in a similar way as [20].

To derive the magnetic circuit model, the geometry of the transformer is separated into divisions along the vertical axis. Fifteen divisions of type 1 have been defined, the position of which are highlighted in Fig. 11a in blue color divided by dashed lines. All of this type of divisions have the same height equal to $h_{Div1} = 49mm$, each one includes one section of the three core limbs, one complete secondary winding, as well as one section of the primary winding of three phases. The division contains the secondary winding $W_{s,A3}$ is taken out from the transformer geometry as an example, the magnetic circuit of which shown in Fig. 11b is established resembling the physical geometry slice (above the magnetic circuit in the same figure, view from the top and front). This magnetic circuit inherits the structure proposed by [20] as an extension into three phase. The three permeance blocks filled with solid color represent flux path inside the transformer core, the value of which can be calculated as

$$P_{C,Mid} = \mu_C \cdot A_C / h_{Div1} \qquad (17)$$

Compared to the ideal model described in section II, the core permeances $P_{C,limb}$ representing the whole limb in Fig. 4b are now distributed into different divisions. Besides the core permeances, the other permeance blocks P_s, P_{long} and P_{shunt} represent the leakage flux path through the air, following the definition made in section III. They can be parametrised using only a few number of experimental tests, which is discussed later. Thanks to the approximately identical geometry, the magnetic circuit of all 15 divisions can share the same permeance values P_{c1}, P_s, P_{long} and P_{shunt}. One should pay attention that, in comparison to the structure of single phase transformer presented in Fig. 7b, the additional horizontal permeance between the two side limbs stands for the inter-phase leakage flux coupling, the value is one half of the others, that is $0.5 P_{shunt}$. The factor 0.5 is applied due to the fact that the magnetic path length between the two side limbs can be considered to be twice of the one between the middle- and side limb, and the permeance value is inversely proportional to the magnetic path length.

Each phase of the primary winding has $N_p = 323$ turns in total and the overall height is $h_{Wp} = 734mm$. The turns number of the primary winding block distributed in each of the type 1 division (except for the one including W_{sA1}) can be approximated as the total number of turns multiplied by the ratio between the height of division and the height of the whole primary winding.
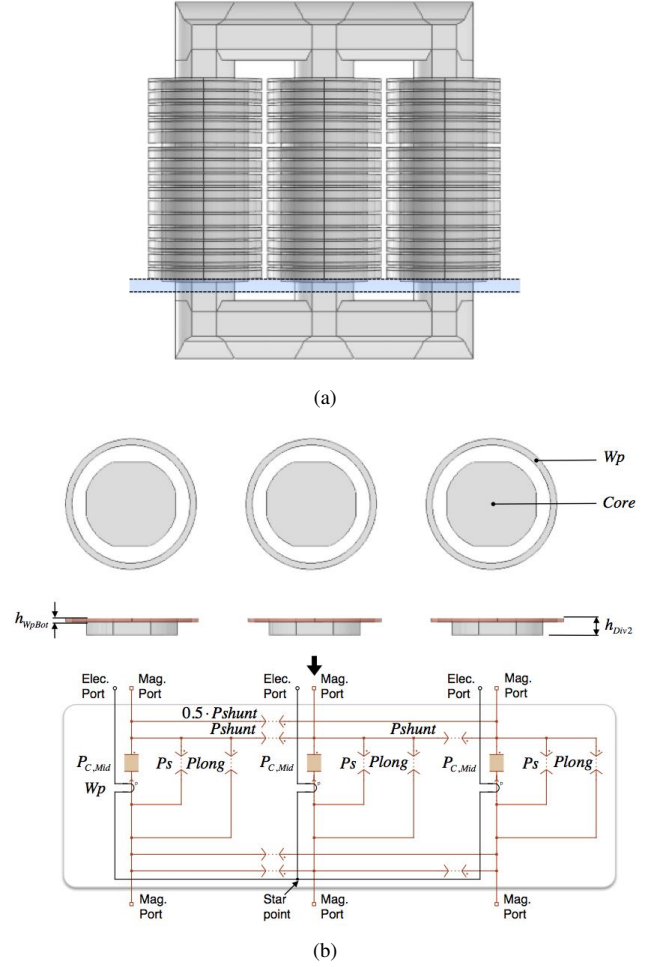

(a)

(b)

Fig. 13: Divisions of type 2 (a) Position in the complete transformer; (b) Cross section and permeance magnetic circuit with the flux path of the core and air.

$$N_{p,Div1} = N_p \cdot h_{Div1} / h_{Wp} = 21.6 \qquad (18)$$

Special attention needs to be paid on the geometrical asymmetries, which was not covered by the work of [20] and is discussed in the following part of this section:

The first kind of asymmetry is the unaligned vertical position of the primary winding with respect to the secondary windings, which is firstly reflected in the division containing W_{sA1} located on the very top of all other secondary windings. As shown in Fig. 12, the primary winding section in this division spans from the bottom only up to $h_{Wp,Top} = 32.5mm$, which is lower than the total height of the whole division h_{Div1}. Following the same idea of equation (18), the primary winding component in this division should be calculated as:

$$N_{p,Div1Top} = N_p \cdot h_{WpTop} / h_{Wp} = 14.3 \qquad (19)$$

In this way, $N_{p,Div1Top}$ becomes lower than $N_{p,Div1}$.

Attached to the type 1 division containing the secondary winding W_{sC1}, one division of type 2 is defined as highlighted in Fig. 13a, where the primary winding is partly out of
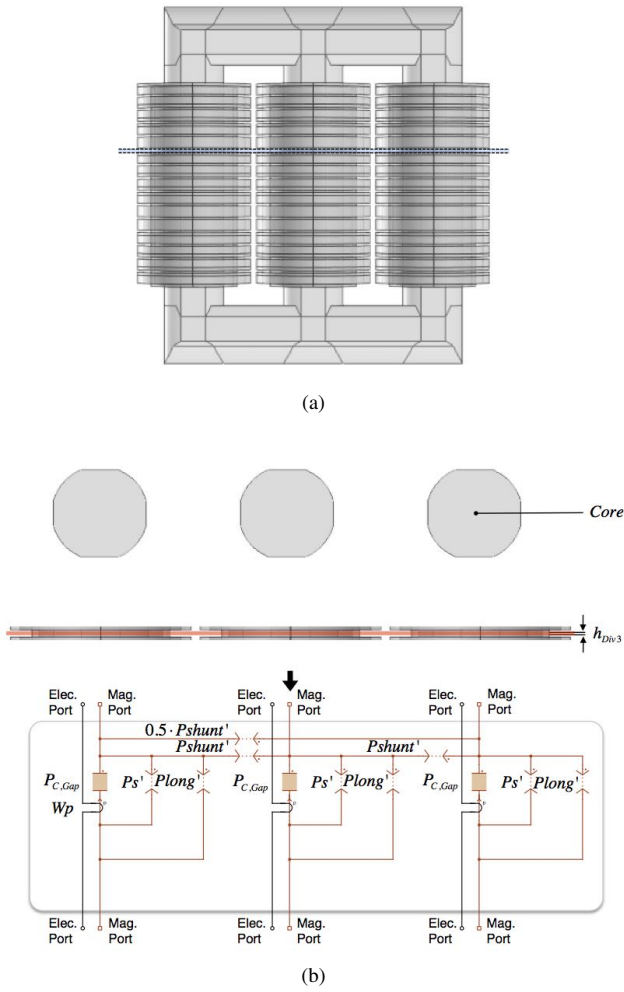
(a)

(b)

Fig. 14: Divisions of type 3 (a) Position in the complete transformer; (b) Cross section and permeance magnetic circuit with the flux path of the core and air.

the vertical range of the secondary windings. The magnetic circuit of this division is demonstrated in Fig. 13b, which has similar structure as that in Fig. 11b, except for the absence of secondary winding. The height h_{Div2} of this section is selected to be equal to that of the division type 1, so that the permance blocks representing the core and leakage flux path have the same value as in division type 1. In the real transformer, the three phases of the primary winding are in star connection and the start point is located at the bottom, thus the low-side electrical port of the three primary winding components in this division are connected together. Similar to the type 1 division including W_{sA1}, here the height of the primary winding section h_{WpBot} is also significantly lower than the division height h_{Div2}. Therefore the turns number of the primary winding block in this division should be calculated proportional to the height as well.

$$N_{p,Div2Bot} = N_p \cdot h_{WpBot}/h_{Wp} = 3.3 \qquad (20)$$

The second kind of asymmetry is reflected on the gaps between the windings, which are defined to comply with

dielectric requirements. The windings belonging to the same output phases (A, B or C) are placed close to each other, with a small gap in between. The windings in output phase "C" are arranged up-side-down in comparison to phase "A" and "B", so that W_{sB5} and W_{sC5} locate directly next to each other. Since the output terminal of the power cells supplied by W_{sB5} and W_{sC5} are both connected to the star point of the load, the voltage stress between these two secondary windings is the same as that inside one output phase, so that the same gap can be applied. In comparison, W_{sA5} has to be kept far away from W_{sB1} due to large voltage stress which can be as high as five times of the DC-link voltage, therefore larger gap has been inserted between them. In order to capture the influence of this excessive gap, one extra division of type 3 is defined between W_{sA5} and W_{sB1}, as highlighted in Fig. 14b. The height of this extra gap division is equal to $h_{Div3} = 8mm$ and the magnetic circuit model is depicted in Fig. 14b. Similar to the division of type 2, the magnetic circuit of the gap division only contain primary winding blocks. One should pay attention that the height of this division is not the same as type 1 and 2, so that the permeance values $P_{C,Mid}$, P_s, P_{long} and P_{shunt} can not be applied here directly. Considering the fact that the leakage permeance value is also proportional to the cross-section area and inverse proportional to the magnetic path length, P_s', P_{long}' and P_{shunt}' can be approximated as scaling of P_s, P_{long} and P_{shunt} about the geometry. The vertical permeance values P_s' and P_{long}' are "inversely" proportional to the division height, while P_{shunt}' is proportional to the division height.

$$P_s' = P_s \cdot h_{Div1}/h_{Div3} \qquad (21)$$

$$P_{long}' = P_{long} \cdot h_{Div1}/h_{Div3} \qquad (22)$$

$$P_{shunt}' = P_{shunt} \cdot \frac{(h_{Div1} + h_{Div3})}{2 \cdot h_{Div1}} \qquad (23)$$

Please note that P_{shunt}' includes the horizontal leakage flux path of not only the gap but also one half of the adjacent type 1 divisions. P_{shunt}' instead of P_{shunt} should be also applied to the horizontal leakage permeance block in the type 1 division which is directly below the gap division containing W_{sB1}. Besides the leakage permeances, the core permeance value $P_{C,Gap}$ in division type 3 can be easily calculated making use of material and geometry information as

$$P_{C,Gap} = \mu_C \cdot A_C/h_{Div3} \qquad (24)$$

Moreover, the turns number of the primary winding block inside this division should be scaled as well, similar to the treatment in the division type 2.

$$N_{p,Div3} = N_p \cdot h_{Div3}/h_{Wp} = 3.5 \qquad (25)$$

The modeling of the rest of the transformer is demonstrated in Fig. 15, including the core yoke as well as the top and bottom part of the limbs. In comparison to the divisions of type 1, since no winding is present in this part of the transformer and the permeability of the main flux path inside the core
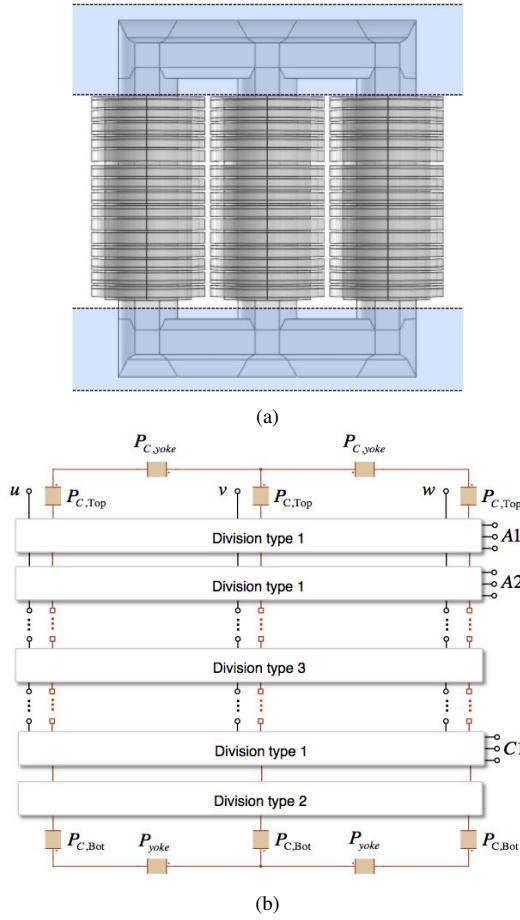
(a)

(b)

Fig. 15: Rest of the transformer geometry outside the winding area (a) Position in the complete transformer; (b) Cross section and permeance magnetic circuit with the flux path of the core and air.

is much more dominant than that of the leakage flux path through the air, the leakage permeances can be neglected. The permeance values of the core blocks here can be calculated using material and geometrical information directly, in the similar way as equation (17). Between these core blocks, the divisions of type 1, 2 and 3 are stacked vertically in succession, and connected via the magnetic- and electrical ports, respectively. This yields the complete circuit model of the transformer, where the electrical terminals of the primary- (with three input phases u, v, w) and the secondary windings can be connected to external circuit, as Fig. 15 demonstrates.

Up to this stage, the core permeance and winding resistances have been determined using geometry and material information explicitly, while the value of the leakage permeances still remain undefined. There are only three parameters P_s, P_{long} and P_{shunt} needed to characterise the whole leakage flux path, which are present in the divisions of type 1, 2, 3. As has been discussed in the previous section, it is difficult to accurately define the geometry of the leakage flux path through the air, therefore a few short-circuit tests are carried out to identify the three unknown parameters, in which one single winding is supplied by voltage source and selected other windings are

short-circuited. Instead of enumerating all the supply-short combinations, only five short-circuit test schemes are needed for the parameter identification which carry sufficient information about coupling between the windings, as recommended by [20].

At first, the equivalent impedance looking into the supplied winding on phase "u" (Fig. 15) is calculated as the peak phase voltage divided by the peak phase current, which is essentially the modulus of the complex impedance, as listed in TABLE III:

TABLE III: Test schemes for leakage permeance parameter fitting

	Supply	Short	Fit to
1	W_p	W_{sA1}	$Z_{k1,Test} = \hat{V}_p / \hat{I}_p / (2\pi f)$
2	W_p	W_{sB3}	$Z_{k2,Test} = \hat{V}_p / \hat{I}_p / (2\pi f)$
3	W_{sA1}	W_{sA2}	$Z_{k3,Test} = \hat{V}_{sA1} / \hat{I}_{sA1} / (2\pi f)$
4	W_{sA1}	W_{sC1}	$Z_{k4,Test} = \hat{V}_{sA1} / \hat{I}_{sA1} / (2\pi f)$
5	W_p	All W_s	$Z_{k5,Test} = \hat{V}_p / \hat{I}_p / (2\pi f)$

After that, the leakage permeance values of the circuit model are fitted to minimise a quadratic objective function, which is the square-summation of the error between the short-circuit inductances from measurement and the one obtained from magnetic circuit simulation of the aforementioned five short-circuit schemes, given by the equation below:

$$f_{obj} = \sum_{i=1}^{5} (\frac{Z_{ki,Test} - Z_{ki,Sim}}{Z_{ki,Test}})^2 \qquad (26)$$

In high power MV transformers, inductive part in the measured short-circuit impedance is usually dominant over the resistive part, due to the less magnetic coupling as a result of the large spacing between windings, which is the case in the phase-shift transformer studied in this work. Therefore the amplitude of the impedance can be directly taken for parameter fitting, without extracting out the inductive component, which is different than the case of low voltage prototype transformer discussed in [20]. Commonly used gradient based- or evolutionary fitting algorithms can be applied to find out the leakage permeance values, iteratively. Generally the fitting process can be carried out in a way demonstrated in Fig. 16. On one side, after receiving the leakage permeance values P_s, P_{long}, P_{shunt} provided by the fitting algorithm before each objective function evaluation, five magnetic circuit models of the transformer which are configured complying to each of the five test schemes specified by TABLE III are simulated in time-domain, one after each other. The simulated time-domain waveforms of winding voltage and current are converted into amplitude, so as to calculate the equivalent impedance values and yields the output of the objective function defined by equation (26). On the other side, the fitting algorithm retrieves the output of objective function from the last evaluation, adjusts the P_s, P_{long}, P_{shunt} values and brings them into the next objective function evaluation.

Initial values need to be assigned in order to make the algorithm better converge, which for the phase-shift transformer can be calculated as below. In certain circumstances the fitting
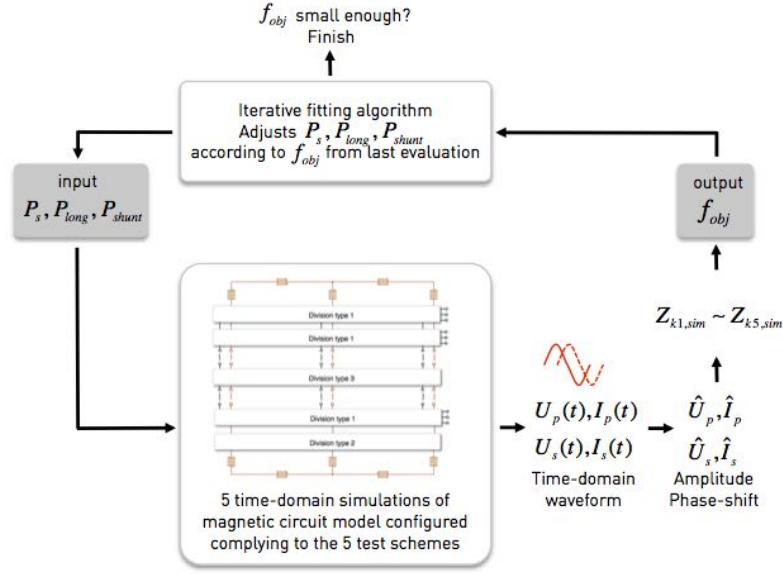
Fig. 16: Generalised fitting process of the leakage permeance values, where the magnetic circuit model is simulated to for calculating the output of the objective function for the fitting algorithm.

algorithm may have difficulty in convergence if P_{long0} is exactly equal to 0, instead a small value of e.g. 10^{-7} can be chosen.

$$P_{s0} = \frac{\mu_0 (2r_{Wp}) d_{PS}}{h_{Div1}} \qquad (27)$$

$$P_{long0} = 0 \qquad (28)$$

$$P_{shunt0} = \frac{\mu_0 (2r_{Wp}) h_{Div1}}{d_{SC}} \qquad (29)$$

The geometrical parameters r_{Wp}, d_{PS} and d_{SC} have been defined in Fig. 11b. Despite of the repetitive structure, thanks to which the whole leakage flux path can be characterised by only three permeance values, strong unbalance of short-circuit impedances will still take place, which will be discussed in the following sections.

V. EXPERIMENTAL VALIDATION WITH SHORT-CIRCUIT TEST

For verification of the proposed modeling's approach, the aforementioned MV phase-shift transformer was experimentally measured. In order to carry out the five short-circuit schemes for model parameter identification and further schemes for validation, a test setup is established as shown in Fig. 17a, which is composed of the following functional units:

- Connection to the $50Hz$ power grid with $400V$ line-to-line RMS voltage
- A variac to generate adjustable sinusoidal voltage source
- Two power analyzers to measure the winding voltage and current

After the five impedance values listed in TABLE III have been obtained, the magnetic circuit models with the structure described in the last section is built up in the system-level

simulation software PLECS (Blockset version) in combination with MATLAB/Simulink. Sinusoidal voltage sources are connected to the winding terminals to emulate the variac output in the test setup. Prior to leakage parameter identification, the permeances representing the iron core have been parametrised directly from geometry and material characteristic. Since the transformer is designed to operate far away from saturation, so that the nonlinearity of the core material has little affect on the measured short-circuit inductances, constant permeability has been assigned to the core permeances. The circuit model which is configured complying to test scheme 1 with the source applied to the primary winding W_p and secondary winding W_{sA1} shorted is demonstrated in Fig. 17b, while the ones for the other four test schemes are established in a similar way.

For parameter identification, the "fminsearch" fitting algorithm provided by MATLAB (referred as unconstrained nonlinear optimisation) is adopted. The setup of the fitting algorithm including writing the customised objective function is carried out in a similar way as has been discussed in [20]. The initial permeance values calculated using equations (27) till (29) as well as the ones obtained after parameter fitting using "fminsearch" algorithm are compared in TABLE IV.

TABLE IV: Leakage permeance values fitted to the measurements [H]

	P_s	P_{long}	P_{shunt}
Initial value	$490 \cdot 10^{-9}$	$100 \cdot 10^{-9}$	$101 \cdot 10^{-9}$
After fitting	$1156 \cdot 10^{-9}$	$111 \cdot 10^{-9}$	$146 \cdot 10^{-9}$

In the first group of verification schemes, the source is connected to the primary winding, meanwhile one single secondary winding is shorted. The short-circuit impedances looking into the primary winding with different secondary windings shorted are compared between measurement and magnetic circuit model in Fig. 18. Although all the secondary
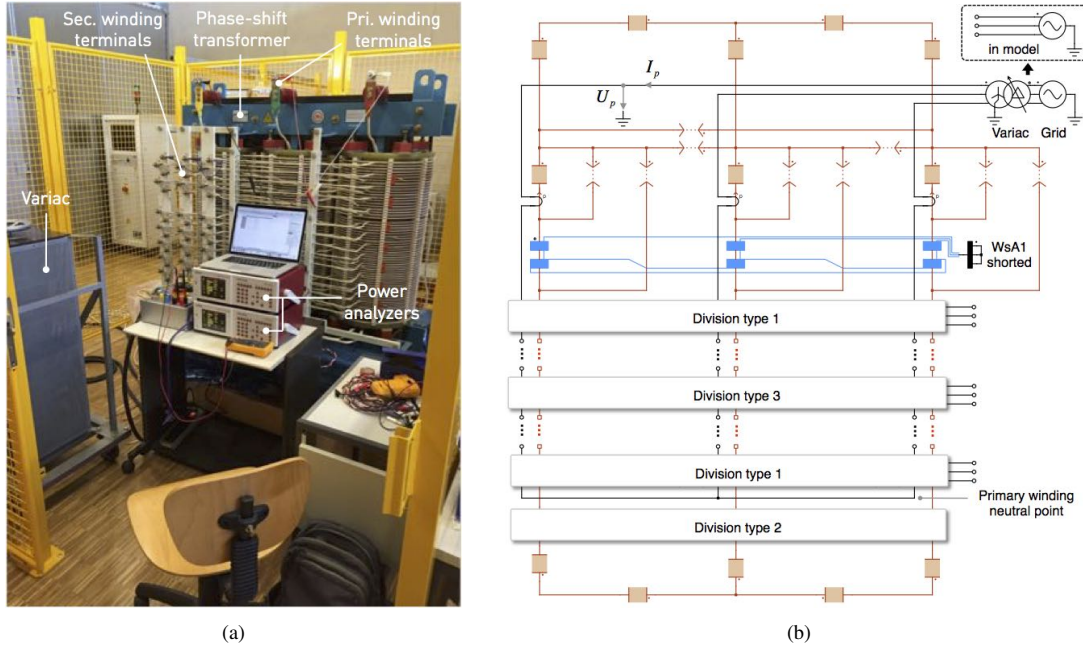
Fig. 17: (a) Short-circuit test setup for the phase-shift transformer, with voltage and current on the supplied winding measured; (b) Magnetic circuit model in PLECS for parameter fitting and verification (test scheme with primary winding supplied and secondary winding W_{sA1} shorted).

windings have approximately the same geometrical dimension and parameterised by repetitive permeance network, the resulted short-circuit impedances however, are unbalanced, due to difference in vertical position with respect to the primary winding. The U-shape curve reveals the fact that the more centralised the secondary winding is located with respect to the primary winding, the stronger is the coupling and thus the lower the short-circuit inductance will be, which has proved the analysis made in the section III. This U-shape curve of short-circuit impedance can be considered to be the reciprocal of the flux curve in Fig. 8b, or in other words, vertically inversed.

Please note that higher impedance is present with the very top secondary winding W_{sA1} shorted than that with the very bottom W_{sC1} shorted, which reflects the effect of the unaligned vertical position of the primary winding with respect

to the secondary windings (demonstrated Fig. 12), this effect has been captured by the model thanks to the turns number adjustment of the primary winding block and the insertion of a type 2 division in the magnetic circuit, as has been discussed in section IV.

The short-circuit impedances in Fig. 18 are obtained making use of the current on phase "u" of the primary winding, in both measurement and simulation. Besides that we have also measured the currents of the other two phases, and the comparison to simulation result in the case with W_{sA1} and W_{sB3} shorted are presented in TABLE V and VI, respectively (rows denoted by "Simulation with $0.5 \cdot P_{shunt}$"). Between the currents from different phases, only slight unbalance can be observed. The good match between measurement and simulation indicates that the inter-phase leakage flux coupling is also well captured, thanks to the permeance $0.5 \cdot P_{shunt}$ inserted between the two
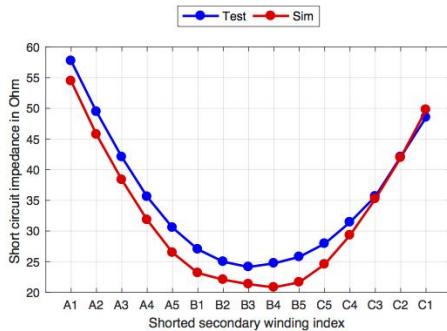

Fig. 18: Short circuit impedances with W_p supplied and different single W_s shorted.

TABLE V: Comparison of three-phase primary winding currents, with W_p supplied and W_{sA1} shorted

RMS current	$I_{p,u}$ [A]	$I_{p,v}$ [A]	$I_{p,w}$ [A]
Measurement	4.0	3.2	3.9
Simulation with $0.5 \cdot P_{shunt}$	4.2	3.1	4.1
Simulation without $0.5 \cdot P_{shunt}$	7.0	3.1	6.4

TABLE VI: Comparison of three-phase primary winding currents, with W_p supplied and W_{sB3} shorted

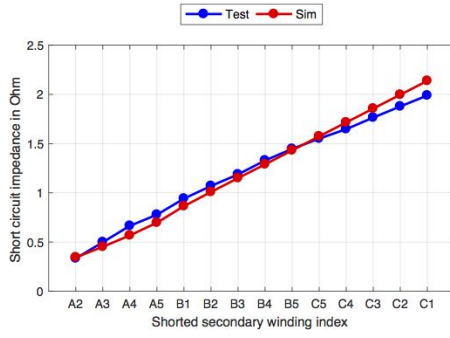| RMS current	$I_{p,u}$ [A]	$I_{p,v}$ [A]	$I_{p,w}$ [A]
Measurement	9.6	8.8	9.2
Simulation with $0.5 \cdot P_{shunt}$	10.8	8.7	9.8
Simulation without $0.5 \cdot P_{shunt}$	13.9	8.7	11.2

Fig. 19: Short circuit impedances with W_{sA1} supplied and one of the other W_s shorted.

side limbs, as demonstrated in Fig. 7b. If the leakage flux coupling between the two side limbs is neglected in the model by removing the $0.5 \cdot P_{shunt}$ permeance, the simulated three-phase currents become strongly unbalanced, the currents on phase "u" and "w" (on side legs) exhibits significant error compared to the measurement, as has also been included in TABLE V and VI (rows denoted by "Simulation without $0.5 \cdot P_{shunt}$"). In the single-phase case discussed in [20], however, since no winding is present on the side limbs, the permeance $0.5 \cdot P_{shunt}$ was not needed.

In the second group of verification schemes, the secondary winding W_{sA1} on the very top is supplied, meanwhile another secondary winding is shorted. The resulted impedances looking into W_{sA1} are shown in Fig. 19 with different other secondary windings shorted. This shape of impedance curve is also correlated to the analysis made in the section III that the further the secondary windings are located from each other, the weaker is the leakage flux coupling in between, which can be regarded as the vertical mirror of the flux curve presented in Fig. 10. From the result comparison one can see that not only the points used for parameter identification (short W_{sA1}, W_{sB3} in Fig. 18 and short W_{sA2}, W_{sC1} in Fig. 19), but also the impedance values of the other verification points match well between the proposed magnetic circuit model (built in PLECS/Simulink) and test result. The maximum error is 16.1% in Fig. 18 and 14.7% in Fig. 19. If the same short circuit tests are applied to the ideal model described in section II, the simulated short circuit impedances are constant 23.7Ω and 0.59Ω for the two verification schemes, respectively, which does not match the unbalance measured from experimental setup.

TABLE VII: Winding currents on phase "u" (RMS value) with primary winding supplied, two secondary windings W_{sA1} and W_{sA2} shorted at the same time

	V_p [V]	I_p [A]	I_{sA1} [A]	I_{sA2} [A]
PLECS	232	5.12	18.2	26.3
Test	232	4.80	16.3	24.8
Error		6.6%	11.7%	6.0%

In the third group of verification schemes, the primary winding is supplied with other two secondary windings shorted

TABLE VIII: Windings currents on phase "u" (RMS value) with primary winding supplied, two secondary windings W_{sA1} and W_{sC1} shorted at the same time

	V_p [V]	I_p [A]	I_{sA1} [A]	I_{sC1} [A]
PLECS	76.2	4.88	19.3	20.6
Test	76.2	4.33	17.4	19.9
Error		12.7%	10.9%	3.5%

at the same time. The short-circuit combination together with the short circuit currents are listed in TABLE VII and TABLE VIII. Good match between magnetic circuit model and the measurement is present here as well with maximum error of 12.7%.

The fourth verification scheme is the same as the fifth test scheme for parameter identification, where the primary winding is supplied by $133V$ line-to-line (RMS) voltage and all the secondary windings are shorted at the same time. Here the current on each of the secondary windings is measured, and compared between test measurement and simulation in Fig. 20. Obvious unbalance is present on the secondary winding currents and the simulation model is able to reproduce it with good accuracy, the maximum error is 15.1%. The influence of the vertically shifted primary winding with respect to the secondary windings, which has been discussed in the modeling
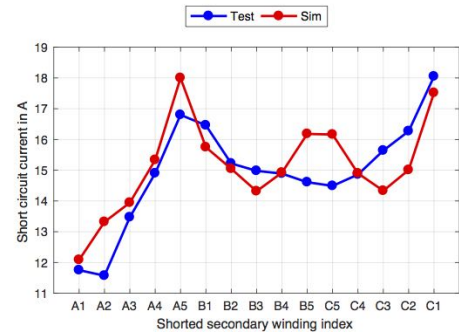

Fig. 20: Short circuit currents with W_p supplied and all of the W_s shorted at the same time.
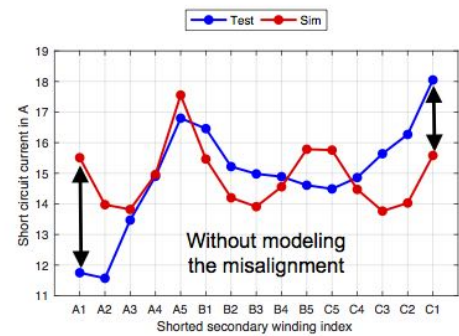

Fig. 21: Short circuit currents with W_p supplied and all of the W_s shorted at the same time, neglecting the vertical position misalignment between primary- and secondary windings in the model.
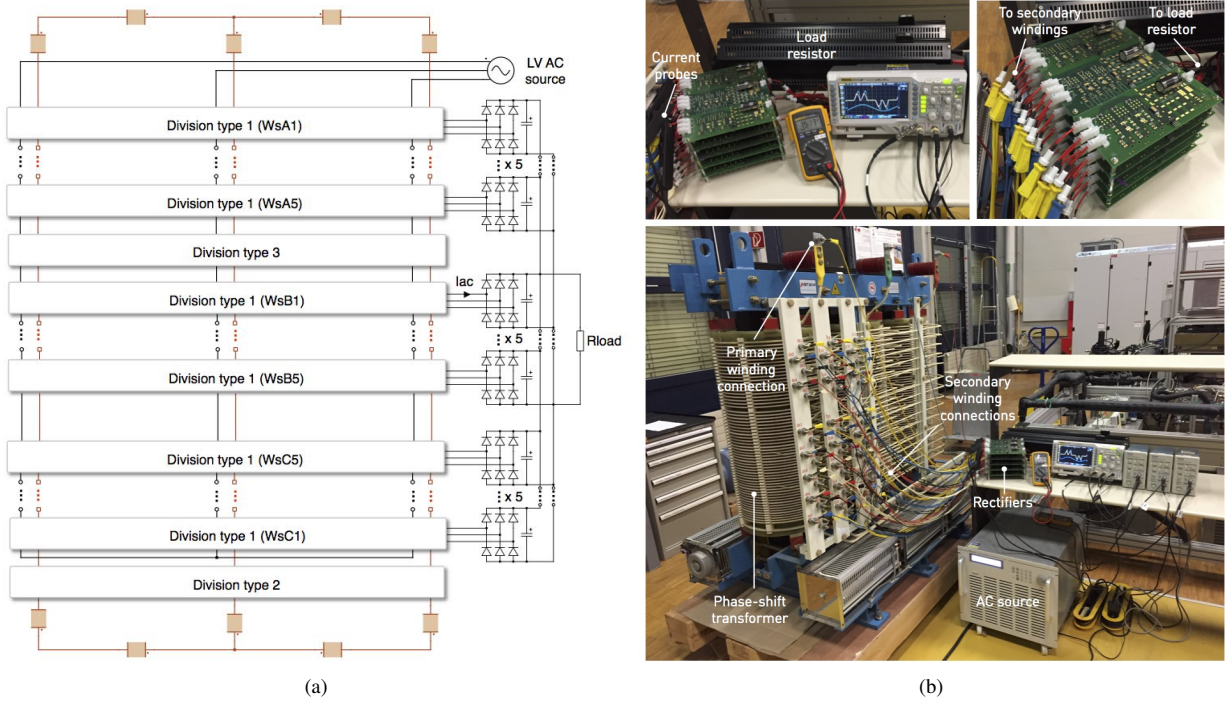
Fig. 22: Verification setup with the primary winding of the transformer supplied by AC source, and secondary windings feeding 15 diode rectifiers connected to a common resistive load: (a) Schematic and system-level simulation model; (b) Hardware configuration.

of the type 1 division with W_{sA1} as well as the type 2 division, can be observed here. This result in significantly reduced current on W_{sA1} and increased current on W_{sC1}, in comparison to the other secondary windings. However, if we neglect this misalignment in geometry by removing the division type 2 and set the primary winding turns number of the very top type 1 division to be identical as the others, the current of W_{sA1} and W_{sC1} becomes nearly equal to each other, which result in obvious discrepancy to the measurement, as demonstrated in Fig. 21. Again in the single phase case discussed in the work of [20], this misalignment did not exist in the prototype transformer and thus was not included in the model.

Moreover, the extra gap between W_{sA5} and W_{sB1} is showing its influence on the secondary current distribution, which boosts the current on W_{sA5} obviously. This effect has been captured by the model as well, thanks to the insertion of a gap division (Fig. 14) in the magnetic circuit.

VI. EXPERIMENTAL VALIDATION WITH DIODE RECTIFIERS

In this section, the fidelity of the proposed transformer model with connection to power electronic converters is verified. Due to lack of access to a CHB converter power hardware in the original MV application, the experimental test is conducted in combination with low-voltage (LV) diode rectifiers, which are designed to support experimental investigations.. Considering the fact that the leakage fluxes flow through the air, whose magnetic characteristic is linear and independent of the excitation amplitude, the LV setup should be also able to

capture the unbalance in leakage flux coupling that originally take place in MV operation.

The schematic and hardware configuration of the verification setup is demonstrated in Fig. 22b: The primary winding is supplied by $50Hz$ balanced three-phase AC voltage generated by the grid emulator from Chroma (type 61700), while the secondary windings are connected to 15 identical three-phase diode rectifiers. Each rectifier is equipped with a $150\mu F$ capacitor on the DC side. In order to observe the influence exclusively from the unbalanced leakage flux coupling and simplify overall test setup, the DC output terminals of all rectifiers are connected in parallel on one load resistor of $R_{load} = 4.5\Omega$, so that all rectifiers share the same output DC voltage. Due to the dominant leakage flux path of the secondary windings as well as line frequency excitation ($50Hz$), the effect of the stray inductance as well as capacitance of the long cables connecting the transformer and the rectifiers can be neglected.

The line-to-line RMS voltage of the AC source is configured to be $104V$, which result in a output DC voltage of $15V$ after rectification. The system level simulation model (the magnetic circuit of the divisions are hidden in encapsulated blocks) shown in Fig. 22a has been established in PLECS/Simulink, which includes the transformer model discussed in the previous section. For the sake of fast system-level simulation, all the rectifier diodes are modelled as ideal components. The other parameters of the simulation model (e.g. load resistance) are configured complying with the test hardware.

In Fig. 23a, the AC current (phase "u") on the secondary windings W_{sA1}, W_{sB1} and W_{sC1} from measurement and
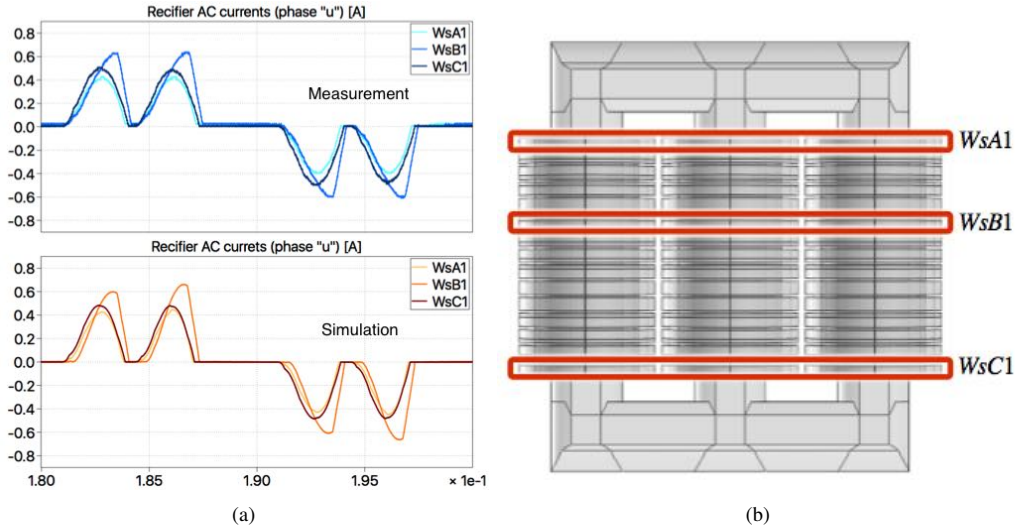
Fig. 23: (a) Measured and simulated rectifier AC currents on W_{sA1}, W_{sB1} and W_{sC1} (phase "u"); (b) Position of the secondary windings W_{sA1}, W_{sB1} and W_{sC1} on the transformer core.
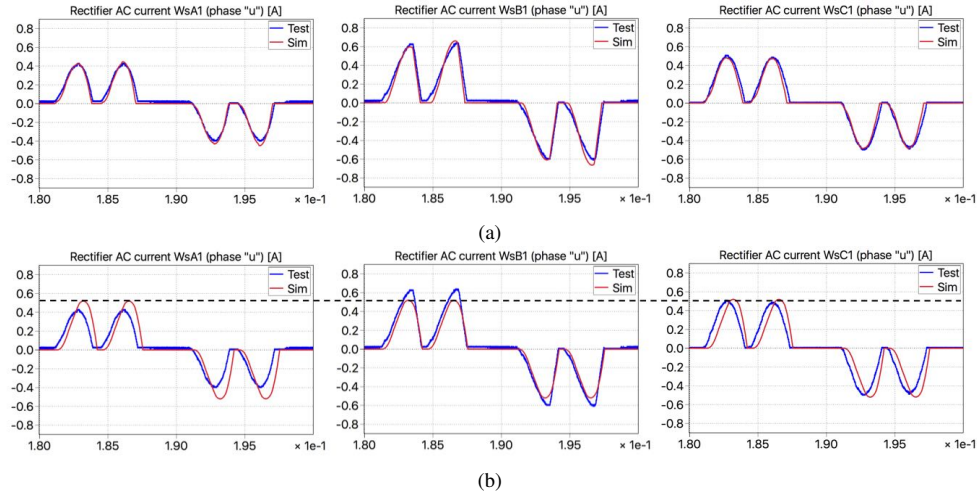

Fig. 24: Comparison between measured and simulated currents on W_{sA1}, W_{sB1} and W_{sC1} (phase "u") (a) using proposed model with unbalanced leakage flux coupling; (b) using ideally balanced leakage inductance model.

simulation are displayed in two separate plots, respectively. Although these three windings have exactly the same turns number configuration and the DC voltage for their rectifiers are also identical, the measured AC current on W_{sB1}, however, has significantly higher amplitude than that on W_{sA1} and W_{sC1} (blue curves). This unbalance can be ascribed to the nonidentical leakage flux coupling to the primary winding, as the consequence of the different vertical position of these windings, as shown in Fig. 23b. This unbalance has been well captured by the simulation model (red-orange curves), thanks to the proposed approaching in representing the leakage flux path. A finer comparison between measurement and simulation has been made in Fig. 24a for the AC currents on W_{sA1}, W_{sB1} and W_{sC1}, respectively, where the simulation result exhibits only slight discrepancy to the measurement. The maximum error of the RMS value is 8% on W_{sC1}.

If the part of transformer model is replaced by the one with

ideally balanced secondary leakage inductance introduced in section II, the current waveforms on W_{sA1}, W_{sB1} and W_{sC1} becomes exactly the same, as shown in Fig. 24b. Without taking into account the unbalanced leakage flux coupling, the simulated current waveforms from the ideal model exhibits significant discrepancy on both amplitude and phase, in comparison to the measurement. The maximum error of the RMS value turns out to be 26.8% on the very-top secondary winding W_{A1}.

Different from the secondary windings W_{sA1}, W_{sB1} and W_{sC1}, the vertical positions of W_{sA5}, W_{sB5} and W_{sC5} (same turns number configuration) are closer to each other (Fig. 25b) on the transformer core, which makes the AC currents better balanced among these three windings, as the measurement result in Fig. 25a illustrates. This reduced unbalance can be observed in the simulation result as well. As has been compared in Fig. 26, the simulation model is still able to
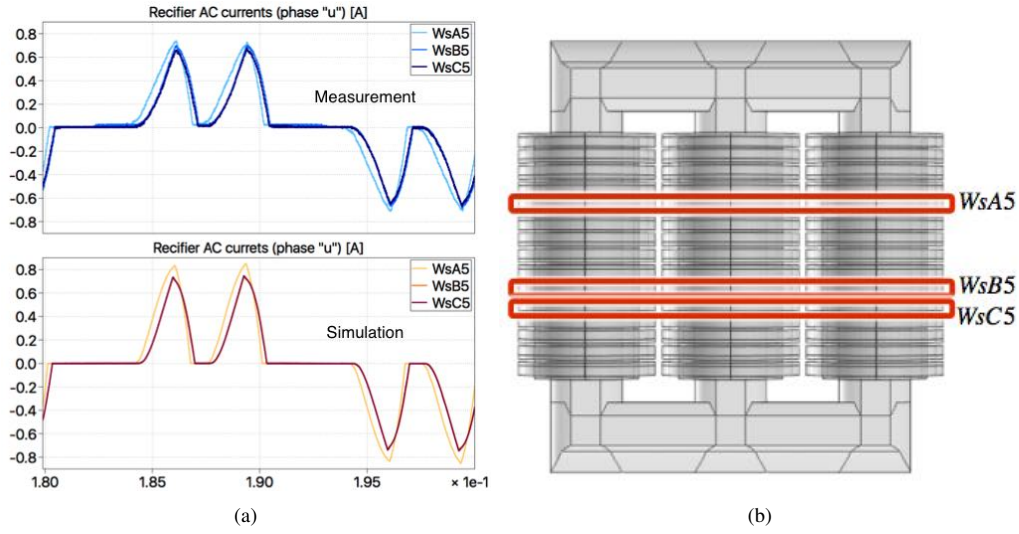
(a)   (b)

Fig. 25: (a) Measured and simulated rectifier AC currents on W_{sA5}, W_{sB5} and W_{sC5} (phase "u"), where the currents on W_{sB5} and W_{sC5} nearly overlap with each other; (b) Position of the secondary windings W_{sA5}, W_{sB5} and W_{sC5} on the transformer core.
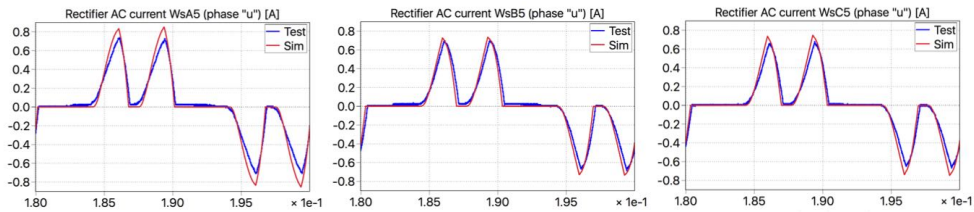

Fig. 26: Comparison between measured and simulated secondary winding currents on W_{sA5}, W_{sB5} and W_{sC5} (phase "u").

reproduces the measurement with good accuracy.

Finally, the comparison of the AC currents' RMS value on all the secondary windings are presented in Fig. 27, strong unbalance can be observed. Please note that if the DC outputs of the rectifiers are isolated from each other, as is the case in the CHB converters, the unbalance present in the rectifier AC current of individual secondary windings will directly lead to unbalanced ripple current on the individual DC-link capacitors, as will be discussed in the next section. Since ripple current is directly related to the lifetime of the capacitors [6], this

Fig. 27: Comparison of the AC currents' RMS value among all secondary windings between test measurement and simulation.

unbalance will make some of the capacitors age faster than the other and thus potentially add up to the difficulty in arranging a maintenance plan.

VII. PERFORMANCE IN SYSTEM LEVEL SIMULATION

After the magnetic circuit model of the transformer has been verified by the short circuit test results and that with diode rectifier connection, further evaluations are carried out in system level simulation environment under MV excitation. Comparison is made between the simulated performance with balanced and the identified unbalanced leakage parameters.

In the first evaluation scheme, the primary winding is supplied by three-phase 50Hz sinusoidal voltage source which emulates the MV grid connection. The line-to-line RMS voltage is equal to $6.3kV$ and the grid internal impedance is neglected. All secondary windings are connected to identical full-bridge diode rectifiers. The output of the diode rectifiers are connected to constant DC voltage sources, the voltage of which are all equally configured to $970V$, the ratio between DC voltage and the primary AC voltage is the same as that of the LV experimental verification setup in the last section. Apart from the connection of the hardware test presented in the previous section VI, the DC outputs of the rectifiers here are isolated from each other, so that the ripple current of individual DC source can be accessed. The system level simulation model including the transformer is shown in Fig. 28.
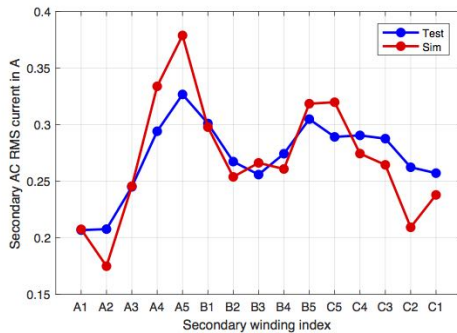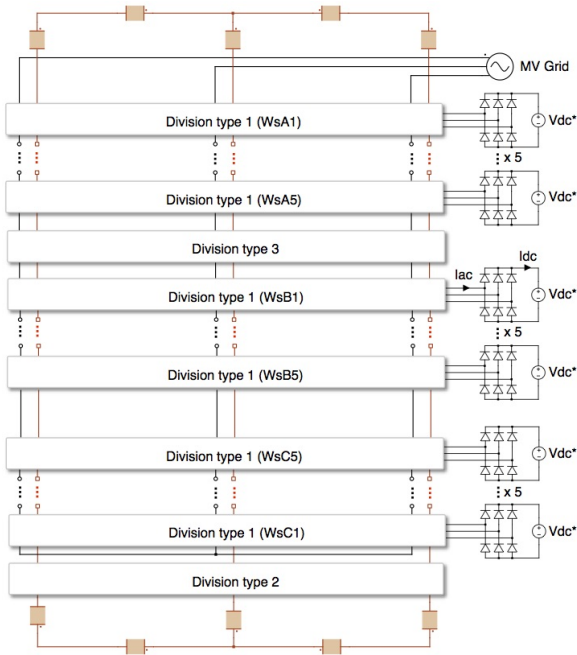
Fig. 28: System-level simulation model with MV grid as input and diode rectifiers connected to constant DC voltage sources as output.

In order to explore the influence from the unbalanced leakage flux path, the transformer model with ideally balanced leakage inductances described in section II is also connected to diode rectifiers in the same way as Fig. 28, for further comparison.

In the upper plots of Fig. 29a and Fig. 29b, the simulated AC current I_{ac} of phase "u" (as has been denoted in Fig. 28) on the secondary windings W_{sA1}, W_{sB1} and W_{sC1} from unideal- and ideal model are compared with each other. In the unideal model, although these three windings have totally the same phase-shift configuration and the same winding geometry, due to the different position on the transformer core however, obvious difference can be observed between their AC currents in Fig. 29a. It is also to be noted that the shape of the AC side current present in Fig. 29a is essentially a linear scaling of that in Fig. 23a from the last section, due to the fact that the AC input- and DC output voltage of the MV simulation are scaled up with the same factor from that of the LV experimental setup. After rectification, the ripple currents $\widetilde{I}_{dc}$ (with the DC component removed from the DC source current) on the DC side also exhibit noticeable unbalance, as shown in the lower plots from Fig. 29a. Since the short-circuit impedance from primary winding to the secondary winding W_{sB1} is smaller than that to W_{sA1} or W_{sC1}, as has been demonstrated in Fig. 18, the DC ripple component on W_{sB1} is higher. In comparison, the simulated current from the ideal model nearly overlap with each other, due to the identical series inductance values $\overline{L}_s$, which is not the case with real transformer.

Further in Fig. 30 the RMS value of the DC side ripple current on all the secondary windings are compared between the unideal- and ideal model, and significant unbalance is
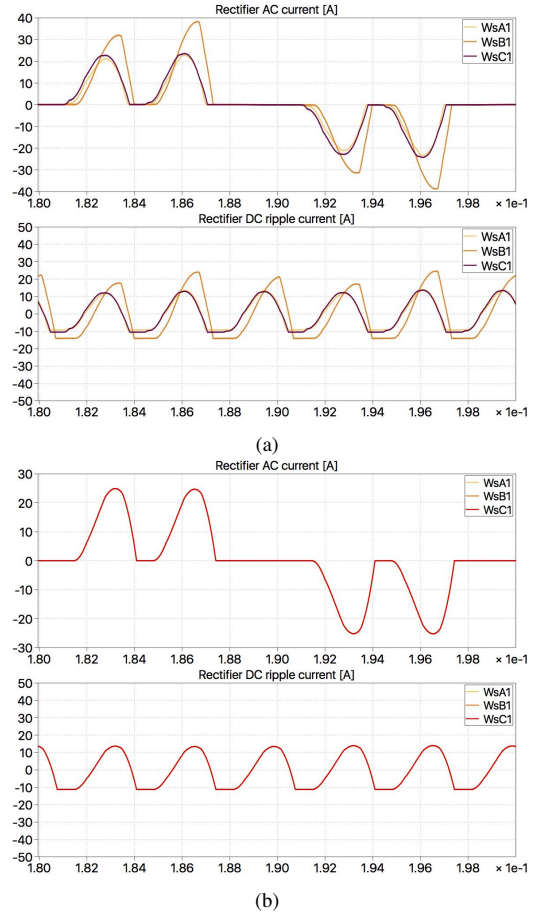

Fig. 29: Simulated time domain waveform of the rectifier side AC current (phase "u") and DC ripple current on the secondary windings W_{sA1}, W_{sB1} and W_{sC1}, with diode rectifier connected to constant voltage sources, from the model (a) with unideal leakage flux path; (b) with idealised leakage inductances.

present in the result of unideal model. The ratio between the highest- and lowest RMS ripple current in the ideal model is 1.24, while in the unideal model it is 1.91.

In the second evaluation scheme, the complete power cells including the diode rectifier, DC-link capacitor and H-bridge IGBT inverter are connected to the secondary windings. The DC link capacitors are configured to be $3mF$. The H-bridges are cascaded in the output phases to drive a three-phase R-L load with resistance $R_{load} = 30\Omega$ and inductance $L_{load} = 10mH$. The complete simulation model with the transformer model including unbalanced leakage flux path is demonstrated in Fig. 31. The model with idealised leakage inductances is reconfigured in the same way. The H-bridges are controlled in a open-loop way using interleaved carrier PWM modulation of switching frequency $500Hz$ and peak modulation index equal to 1. The simulated primary winding current I_p, multi-level inverter output voltage V_{out} as well as output current I_{out} from the unideal- and ideal model are shown in Fig. 32a and 32b, respectively. Thanks to the phase-shifted winding configuration, the primary winding currents flowing out of
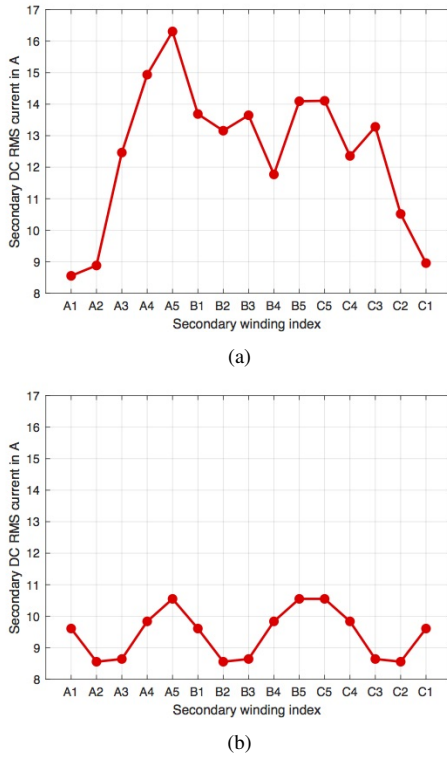
(a)

(b)

Fig. 30: Simulated RMS value of the rectifier side DC ripple current on all the secondary windings, with diode rectifier connected to constant voltage sources, from the model (a) with unideal leakage flux path; (b) with idealised leakage inductances.
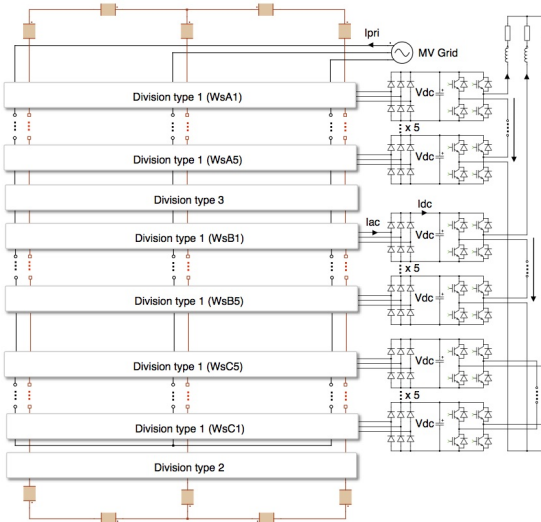

Fig. 31: System-level simulation model with MV grid as input and complete power cells driving three-phase RL load.
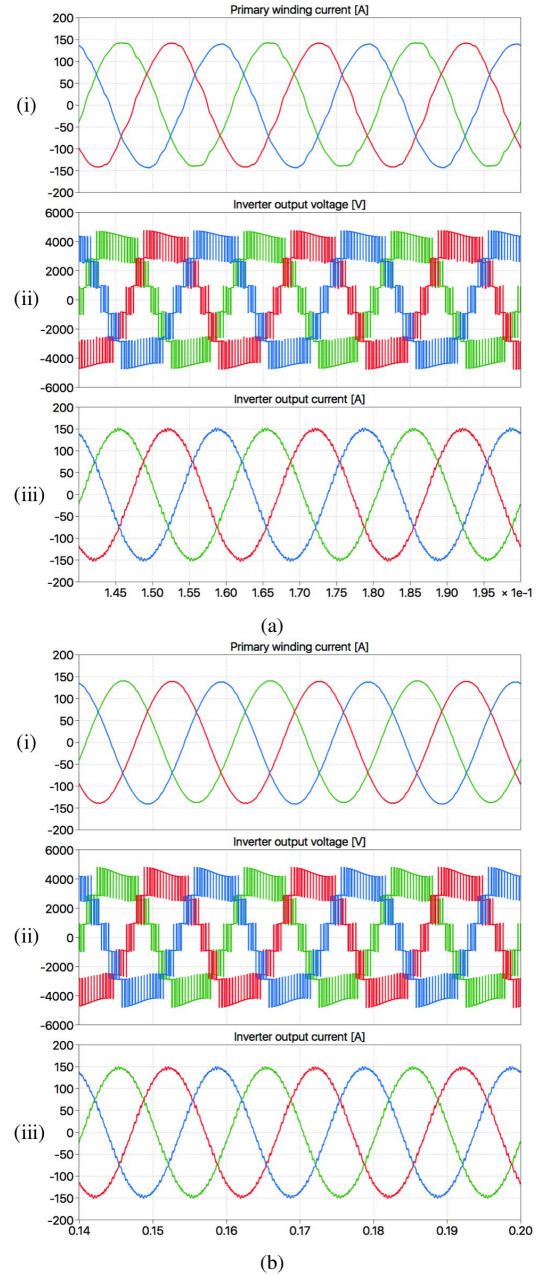

(a)

(b)

Fig. 32: Simulated time domain waveform of the primary current, inverter output voltage and inverter output current from the model using complete power cells (a) with unideal leakage flux path; (b) with idealised leakage inductances.

the MV-grid become approximately ideal sinusoidal wave. Slightly higher harmonic component can be observed on the simulated result from the unideal model, as a result of the unbalanced leakage flux paths.

On the inverter output side, the voltage and current wave-forms are almost the same between the unideal- and ideal models, due to the fact that the DC-link capacitors have decoupled the voltage source inverter from the transformer unbalance. However on the diode rectifier side of the DC-link capacitors, the simulated ripple current of secondary windings W_{A1}, W_{B1} and W_{C1} from the unideal model shown in Fig. 33a exhibits even stronger unbalance, in comparison to Fig. 29a. If the RMS ripple current of all the secondary windings are compared together in Fig. 34a, the ratio between the highest- and lowest value becomes 2.7, which is significantly
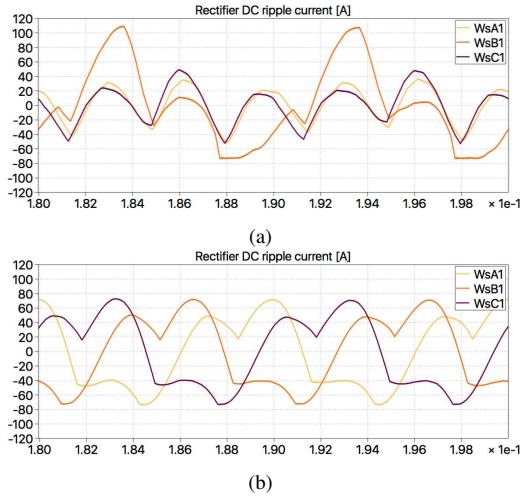
Fig. 33: Simulated time domain waveform of the rectifier side DC ripple current on the secondary windings W_{sA1}, W_{sB1} and W_{sC1} from the model using complete power cells (a) with unideal leakage flux path; (b) with idealised leakage inductances.

Fig. 34: Simulated RMS value of the rectifier side DC ripple current on all the secondary windings from the model using complete power cells (a) with unideal leakage flux path (b) with idealised leakage inductances.

higher than that in Fig. 30a. The increased unbalance on rectifier side ripple current can be ascribed to the ripple voltage on the DC-link capacitors (Fig. 35a), which is not present in the first evaluation case. On the ideal model, however, the
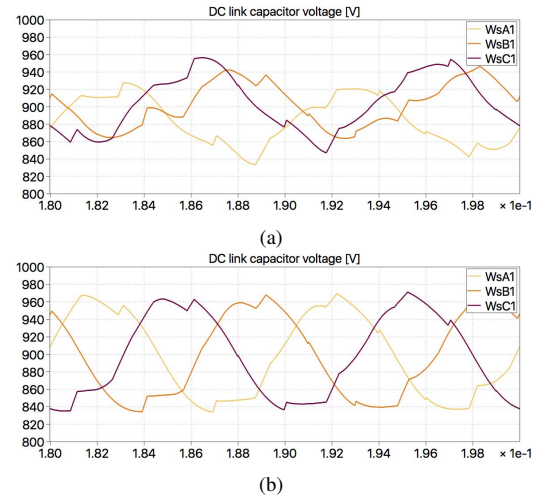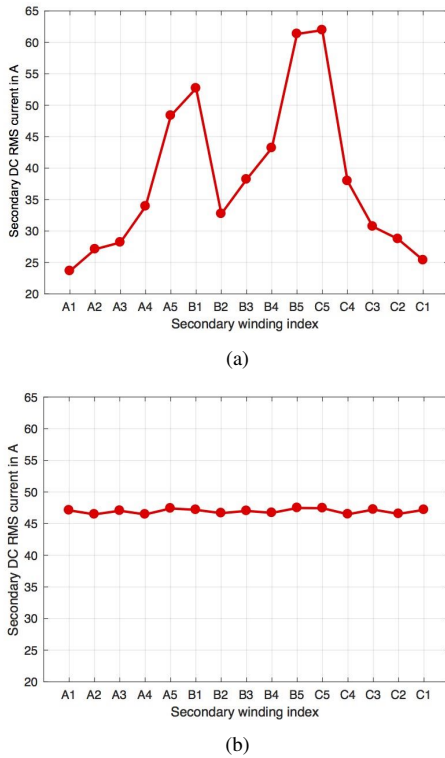

Fig. 35: Simulated time domain waveform of the DC link capacitor voltage of the power cells on the secondary windings W_{sA1}, W_{sB1} and W_{sC1} from the model using complete power cells (a) with unideal leakage flux path; (b) with idealised leakage inductances.

ripple currents on the rectifier side are still well balanced as shown in Fig. 33b and Fig. 34b.

From the result of unideal model, the current on the secondary windings are significantly different from each other, which makes the rectifier diodes unequally loaded. Besides that, the unbalance on the DC side ripple current lead to different stress on the DC-link capacitors. Making use of the simulation result from the proposed transformer model, one would be able to better predict the stress on switching devices and passive components, or improve the modulation strategy on the inverter side to compensate the unbalance. This however, can not be achieved using the ideal model with balanced leakage inductances.

VIII. CONCLUSION

This paper has demonstrated the modelling of phase-shift transformer in MV power converter application using permeance-capacitance based magnetic circuit. The proposed model has the potential to reproduce circuit issues related to the unbalance in leakage flux coupling when integrated into system-level simulation combined with power converters. Via making use of information about the repetitive and symmetrical geometry, the parameters of the leakage flux path can be obtained from only a few experimental tests. The result from the proposed model shows good match to the hardware test, under a plenty of short-circuit schemes. In comparison to the conventional model with ideally balanced leakage inductance, the proposed model is able to reproduce effects that arise from the unbalanced leakage flux path. The simulation result may potentially help with component selection as well as developing the control algorithm of the whole converter system.

REFERENCES

[1] J. Rodriguez, S. Bernet, B. Wu, J. O. Pontt, and S. Kouro, "Multlevel voltage-source-converter topologies for industrial medium-voltage drives," in *IEEE Transactions on Industrial Electronics*, vol. 54, 2007, pp. 2930–2945.

[2] P. W. Hammond, "A new approach to enhance power quality for medium voltage ac drives," in *IEEE Transactions on Industry Applications*, vol. 33, no. 1, 1997, pp. 202–208.

[3] J. Rodriguez, P. W. Hammond, J. Pontt, R. Musalem, P. Lezana, and M. J. Escobar, "Operation of a medium-voltage drive under faulty conditions," in *IEEE Transactions on Industrial Electronics*, vol. 52, no. 4, 2005, pp. 1080–1085.

[4] Z. Zheng, Z. Gao, C. Gu, L. Xu, K. Wang, and Y. Li, "Stability and voltage balance control of a modular converter with multiwinding high-frequency transformer," in *IEEE Transactions on Power Electronics*, vol. 29, no. 8, 2014, pp. 4183–4194.

[5] L. Sun, Z. Wu, W. Ma, X. Fei, X. Cai, and L. Zhou, "Analysis of the dc-link capacitor current of power cells in cascaded h-bridge inverters for high-voltage drives," in *IEEE Transactions on Power Electronics*, vol. 29, no. 12, 2014, pp. 6281–6292.

[6] M. A. Vogelsberger, T. Wiesinger, and H. Ertl, "Life-cycle monitoring and voltage-managing unit for dc-link electrolytic capacitors in pwm converters," in *IEEE Transactions on Power Electronics*, vol. 26, no. 2, 2011, pp. 493–503.

[7] J. van Vlerken and P. G. Blanken, "Lumped modelling of rotary transformers, heads and electronics for helical-scan recording," in *IEEE Transactions on Magnetics*, vol. 31, no. 2, 1995, pp. 1050–1055.

[8] L. Guasch, F. Corcoles, and J. P. L. Sainz, "Effects of symmetrical voltage sags on three-phase three-legged transformers," in *IEEE Transactions on Power Delivery*, vol. 19, no. 2, 2004, pp. 875–883.

[9] A. Davoudi, P. L. Chapman, J. Jatskevich, and A. Khaligh, "Reduced-order modeling of high-fidelity mangetic equivalent circuits," in *IEEE Transactions on Power Electronics*, vol. 24, no. 12, 2009, pp. 2847–2855.

[10] A. D. Theocharis, J. Milias-Argitis, and T. Zacharias, "Three-phase transformer model including magnetic hysteresis and eddy currents effect," in *IEEE Transactions on Power Delivery*, vol. 24, no. 3, 2009, pp. 1284–1294.

[11] P. S. Moses, M. A. S. Masoum, and H. A. Toliyat, "Dynamic modeling of three-phase asymmetric power transformers with magnetic hysteresis: no-load and inrush conditions," in *IEEE Transactions on Energy Conversion*, vol. 25, no. 4, 2010, pp. 1040–1047.

[12] P. G. Blanken, "A lumped winding model for use in transformer models for circuit simulation," in *IEEE Transactions on Power Electronics*, vol. 16, no. 3, 2001, pp. 445–460.

[13] J. Cale, S. D. Sudhoff, and L.-Q. Tan, "Accurately modeling ei core inductor using a high-fidelity magnetic equivalent circuit approach," in *IEEE Transactions on Magnetics*, vol. 42, no. 1, 2006, pp. 40–46.

[14] C. Alverez-Marino, F. de Leon, and X. M. Lopez-Fernandez, "Equivalent circuit for the leakage inductance of multiwinding transformers: unification of terminal and duality models," in *IEEE Transactions on Power Delivery*, vol. 27, no. 1, 2012, pp. 353–361.

[15] S. Jazebi and F. de Leon, "Experimentally validated reversible single-phase multiwinding transformer model for the accurate calculation of low-frequency transients," in *IEEE Transactions on Power Delivery*, vol. 30, no. 1, 2015, pp. 193–201.

[16] L. Cao and J. Yang, "Linear circuit model of the trhee-phase insulated core transformer power supply," in *IEEE Transactions on Nuclear Science*, vol. 63, no. 1, 2016, pp. 288–296.

[17] F. de Leon and J. A. Martinez, "Dual three-winding transformer equivalent circuit matching leakage measurements," in *IEEE Transactions on Power Delivery*, vol. 24, no. 1, 2009, pp. 160–168.

[18] M. Lambert, M. Matinez-Duro, J. Mahseredjian, F. de Leon, and F. Sirois, "Transformer leakage flux models for electromagnetic transients: Critical review and validation of a new model," in *IEEE Transactions on Power Delivery*, vol. 29, no. 5, 2014, pp. 2180–2188.

[19] M. Lambert, F. Sirois, M. Matinez-Duro, and J. Mahseredjian, "Analytical calculation of leakage inductance for low-frequency transformer modelling," in *IEEE Transactions on Power Delivery*, vol. 28, no. 1, 2013, pp. 507–515.

[20] M. Luo, D. Dujic, and J. Allmeling, "Leakage flux modeling of multiwinding transformers for system-level simulations," in *IEEE Transactions on Power Electronics*, 2017, Early Access.

[21] D. Hamill, "Lumped equivalent circuits of magnetic components: the gyrator-capacitor approach," in *IEEE Transactions on Power Electronics*, vol. 8, 1994, pp. 97–103.

[22] C. Marxgut, J. Muehlethaler, F. Krismer, and J. W. Kolar, "Multiobjective optimization of ultraflat magnetic components with pcb-integrated core," in *IEEE Transactions on Power Electronics*, vol. 28, no. 7, 2013, pp. 3591–3602.
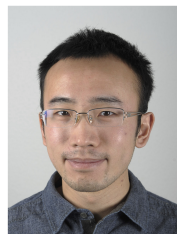
Min Luo Min Luo (M'13) was born in Beijing, China, in 1986. He received the B.S. degree in electrical engineering from Tsinghua University, Beijing, China, in 2009 and M.S. degree in electrical power engineering from RWTH Aachen University, Aachen, Germany, in 2012. Since 2012 he has been with Plexim as application engineer, working on the software PLECS for fast simulation of power electronic systems. In 2014 he joined Power Electronics Laboratory of École Polytechnique Fédérale de Lausanne (EPFL) in Lausanne, Switzerland as external doctoral research assistant, pursuing his PhD degree. His current research interest include dynamic modelling of magnetic components and real-time HIL simulation of power converters.

Drazen Dujic Drazen Dujic (S'03-M'09-SM'12) received the Dipl.-Ing. and M.Sc. degrees from the University of Novi Sad, Novi Sad, Serbia, in 2002 and 2005, respectively, and the Ph.D. degree from the Liverpool John Moores University, Liverpool, U.K., in 2008, all in electrical engineering. From 2002 to 2006, he was with the Department of Electrical Engineering, University of Novi Sad as a Research Assistant, and from 2006 to 2009 with Liverpool John Moores University as a Research Associate. From 2009 till 2013, he was with ABB Corporate Research Centre, Switzerland, as a Principal Scientist working on the power electronics projects spanning the range from low-voltage/power SMPS in below kilowatt range to medium voltage high-power converters in a megawatt range. During 2010-2011, he was a member of a project team responsible for the development of the worlds first power electronic traction transformer (PETT) successfully commissioned on the locomotive. From 2013 till 2014, he was with ABB Medium Voltage Drives, Turgi, Switzerland, as R&D Platform Manager, responsible for ABB's largest IGCT based medium voltage drive - ACS6000. He is currently with Ecole Polytechnique Federale de Lausanne EPFL, Lausanne, Switzerland, as an Assistant Professor and the Director of the Power Electronics Laboratory. His current research interests include the areas of design and control of advanced high-power electronics systems and high performance drives. He has authored or coauthored more than 80 scientific publications and has filed eleven patents. He is an Associate Editor for IEEE Transactions on Industrial Electronics, IEEE Transaction on Power Electronics and IET Electric Power Applications. He has received the First Prize Paper Award by the Electric Machines Committee of the IEEE Industrial Electronics Society at IECON-2007. In 2014 he has received the Isao Takahashi Power Electronics Award for outstanding achievement in power electronics.

Jost Allmeling Jost Allmeling (S'98-M'03) was born in Hamburg, Germany, in 1972. He received the M.S. degree in electrical engineering from Aachen University, Aachen, Germany, in 1996 and the Ph.D. degree from the Swiss Federal Institute of Technology (ETH), Zurich, Switzerland, in 2001. In 1996, he became a Research Associate at the Power Electronics Laboratory at ETH. From 2001 until 2003, he was with the Power Systems Laboratory at ETH, as a Post-Doctoral Researcher. In 2002, Jost co-founded Plexim, a spin-off company from ETH Zurich that develops the software PLECS for fast simulation of power electronic systems. Currently, he is the Managing Director of Plexim. His research interests include simulation of power electronics, modeling electrical and mechanical components, real-time HIL simulation and inverter control.